Atmospheric Research 297 (2024) 107117

Contents lists available at ScienceDirect

Atmospheric Research

journal homepage: www.elsevier.com/locate/atmosres

Impact of PBL schemes on multiscale WRF modeling over complex terrain, Part I: Mesoscale simulations

Yong-Feng Ma [a], Yuting Wang [b,*], Tao Xian [a], Geng Tian [a], Chao Lu [c], Xia Mao [c], Lian-Ping Wang [a]

[a] *Guangdong Provincial Key Laboratory of Turbulence Research and Applications, Department of Mechanics and Aerospace Engineering, Southern University of Science and Technology, Shenzhen 518055, China*
[b] *Department of Civil and Environmental Engineering, the Hong Kong Polytechnic University, Hong Kong 100872, China*
[c] *Meteorological Bureau of Shenzhen Municipality, Shenzhen 518040, China*

ARTICLE INFO

Keywords:
PBL schemes
WRF modeling
Atmospheric boundary layer
Complex terrain
Turbulent heat fluxes

ABSTRACT

This study investigates the performance of two commonly used planetary boundary layer (PBL) schemes, the local turbulence closure (Mellor-Yamada-Janjić: MYJ) and the nonlocal turbulence closure (Yonsei University: YSU), over the tropical coastal region of Shenzhen, China, using the Weather Research and Forecasting (WRF) model. The simulation results are evaluated by comparing them to various measurements. Additionally, we also investigate the performance of the PBL schemes over different land cover types and their ability to reproduce the physical relationships between several pairs of interrelated near-surface atmospheric parameters. The results show that both PBL schemes underestimate temperature and PBL height and overestimate wind speed and turbulent fluxes throughout the whole day, but this can be improved by increasing horizontal resolution. We find that the overestimation of wind speed and turbulent heat fluxes is mainly caused by the strong mechanical mixing in the model. Some improvements are required such as more accurate surface morphology parameters and momentum transport coefficients. Overall, the YSU scheme outperforms the MYJ scheme at all horizontal resolutions over complex terrain in terms of near-surface variables, PBL vertical structures, and the internal relations between turbulent heat fluxes and atmospheric instability. However, the difference between the two PBL schemes, varying over different land covers and with time periods and altitudes within the PBL, is generally greater over the land than over the sea for thermal-related variables (especially during daytime), while for variables associated with water vapor is the opposite. This highlights the importance of the underlying surface for the performance of PBL schemes and the need to select appropriate PBL schemes for simulating the evolution of PBL processes over different land covers.

1. Introduction

The planetary boundary layer (PBL), the lowest part of the troposphere ranging from tens of meters to a few kilometers, is directly influenced by the Earth's surface (Stull, 1988). It responds to various surface forcings (e.g., heat transfer, evaporation and transpiration, frictional drag, pollutant emission and transportation, and terrain-induced flow) within a timescale of about an hour or less (Stull, 1988; Garratt, 1994). The structures and processes of the PBL play a crucial role in the exchange of physical and chemical quantities (e.g., mass, momentum, heat, moisture, and pollutants) between the surface and atmosphere, and thus directly affect weather, climate, and air quality (Garratt, 1994). These exchange processes are generally characterized by transport and mixing associated with turbulent eddies (Konor et al., 2009), which are intrinsic to the boundary layer and constitute the dominant mechanism to transmit surface forcings throughout the entire PBL (Stensrud, 2011). Therefore, accurate modeling of PBL processes, especially boundary layer turbulence, is essential for the numerical simulations of weather, climate, and atmospheric pollutants.

To improve the accuracy of predicting the kinematic and thermodynamics parameters of the atmospheric PBL in numerical weather prediction (NWP) and climate models, turbulent mixing must be reliably represented (Konor et al., 2009; Cohen et al., 2015). However, the resolution of these models is often insufficient to explicitly resolve the structure of PBL turbulence; therefore, empirically tuned and inherently uncertain parameterization schemes are used (Stensrud, 2011; Cohen

---

* Corresponding author.
E-mail address: yuting.wang@polyu.edu.hk (Y. Wang).

https://doi.org/10.1016/j.atmosres.2023.107117
Received 1 August 2023; Received in revised form 28 October 2023; Accepted 18 November 2023

et al., 2015). This approach is known as PBL parameterization, which is usually one-dimensional (1D) and responsible for describing the vertical profiles of the sub-grid-scale (SGS) fluxes due to eddy diffusivity. It provides atmospheric tendencies of temperature, moisture (including clouds), and horizontal momentum throughout the entire atmospheric column (Konor et al., 2009; Skamarock et al., 2019). However, it should be noted that such 1D PBL parameterizations may produce unrealistic flow characteristics in high-resolution mesoscale domains (Zhou et al., 2014; Shin and Dudhia, 2016).

In recent decades, various PBL schemes have been developed to describe turbulent processes in mesoscale atmospheric models (e.g., Mellor and Yamada, 1982; Janjić, 1994; Hong et al., 2006; Pleim, 2007; Bretherton and Park, 2009; Shin and Hong, 2015). For instance, the widely-used mesoscale Weather Research and Forecasting (WRF; Skamarock et al., 2019) model offers >10 PBL schemes. These PBL parameterizations are broadly classified into local and nonlocal turbulence schemes based on their treatment of vertical mixing. Local turbulence schemes consider only the adjacent vertical levels, while nonlocal schemes consider a deeper layer covering multiple levels to represent the vertical mixing effects through the entire PBL (Cohen et al., 2015). It is well understood that the most significant concern with local schemes is their assumption that mixing is related to local turbulent kinetic energy (TKE), which can lead to unrealistic flow characteristics (Zhou et al., 2014). In reality, the vertical mixing throughout the entire PBL is primarily accomplished by the largest eddies, which are often independent of local variations in static stability (Cohen et al., 2015; Stensrud et al., 2015). These large eddies can penetrate the top of the mixed layer and entrain free atmospheric air into the mixed layer, thereby enhancing the PBL depth (Cohen et al., 2015). The nonlocal schemes can better explain the PBL turbulence characteristics and are typically used for convective boundary layers because they account for the counter-gradient fluxes (Stull, 1991; Cohen et al., 2015; Stensrud et al., 2015). However, all local and nonlocal parameterizations rely on several assumptions and may not be well-suited for all environments.

Selecting appropriate PBL parameterizations in NWP and climate models and understanding differences between PBL schemes have been actively studied in recent decades (e.g., Cohen et al., 2015; Jia and Zhang, 2020). Many studies have investigated the sensitivity of PBL parameterizations to meteorological parameters for diverse atmospheric processes, environments, and geographical locations, such as low-level jets (e.g., Ruiz et al., 2010; Santos and Nascimento, 2016), tropical cyclones (e.g., Coronel et al., 2016), mid-latitude cold season severe storms (e.g., Cohen et al., 2015; Pradhan et al., 2019), lightning in hailstorms (e.g., Malečić et al., 2022), warm season mesoscale convective system rainfall (e.g., Jankov et al., 2005), distribution and transport of pollutants (Banks and Baldasano, 2016), the urban heat island (Jandaghian et al., 2018), the PBL structure in stable conditions (Tastula et al., 2015), and weather and climate over the polar regions (e.g., Ma, 2012; Tastula et al., 2012). Interested readers can refer to Cohen et al. (2015) and Jia and Zhang (2020), which provide detailed reviews of the performance of different PBL schemes on meteorological parameters, PBL structures, and turbulence diffusion. Although considerable efforts have been made in previous studies, there is still no unified conclusion on the optimal PBL parameterizations since the performance of different schemes strongly depends on atmospheric conditions, geographical features, model configurations, and time periods (Ruiz et al., 2010; Banks and Baldasano, 2016; Falasca et al., 2021). Therefore, evaluating PBL schemes at different geographical locations and time periods remains necessary.

Unlike most previous studies that focused on mid-latitude continental regions with little or mild topographic variability (see e.g., Jia and Zhang, 2020), this work examines the effects of PBL schemes over the geographically complex tropical coastal region of Shenzhen in the Pearl River Delta (PRD) region of southern China, which encompasses oceans, rivers, reservoirs, mountains, and urban areas. For such complex typography, the vertical SGS fluxes are affected not only by turbulent mixing but also by mesoscale advection processes caused by the surface heterogeneous heating or cooling (Serafin et al., 2018). Although parameterization based on the specific features of a given complex terrain can address this issue, it needs to be established individually for each site and is not universally applicable (Sfyri et al., 2018). Therefore, it is more feasible to investigate and understand the performance of existing PBL schemes over complex terrain and extend these common parameterizations to include the surface heterogeneity effects.

In addition, most previous studies have primarily validated the models using conventional surface meteorological measurements (i.e., surface pressure, 2-m temperature and humidity, 10-m wind speed and direction) and sounding profiles of air temperature, humidity, and winds from low-response sensors (e.g., Ruiz et al., 2010; Xie et al., 2012; Cohen et al., 2015; Jia and Zhang, 2020; Yu et al., 2022), with relatively few verifications with turbulence observations. Moreover, the traditional approach primarily validates individual variables with observed fields, whereas there are intricate interactions between meteorological variables in the PBL. Therefore, this study combines near-surface conventional meteorological observations, sounding profiles, and turbulence measurements to address two questions: (1) What is the performance of different PBL schemes for primary first- and second-order meteorological variables over complex terrain in tropical coastal regions? (2) How well does the WRF model reproduce the basic physical relationships among interrelated near-surface variables?

To answer these questions, we conducted full-physics WRF simulations over the tropical coastal region of Shenzhen, China, using a multidomain nesting approach. The simulations utilizing different PBL schemes were comprehensively validated against multisource observations to provide potential insight into improving PBL parameterizations over complex terrain. The remainder of this paper is organized as follows. In Section 2, we provide details of the near-surface observations and the configurations of the performed simulations. In Section 3, we present the results of our analysis, including model validation with conventional meteorological observations and turbulent measurements, investigation of the sensitivities of the PBL schemes to horizontal resolutions and land cover (LC) types, and evaluation of the ability of the WRF model to reproduce the physical relationships between near-surface variables. Finally, the conclusions are presented in Section 4.

2. Methodology

2.1. Micrometeorological measurements

Shenzhen is a tropical coastal city located in the PRD region of South China, bordered by the Pearl River to the west, Mirs Bay and Daya Bay to the east, and Hong Kong and the South China Sea to the south. Its climate is mainly influenced by the Asian monsoon and local land-sea interactions, representing a typical coastal urban climate with a warm and dry winter, hot and humid summer, as well as some unique local microclimate features (e.g., sea-land breeze, urban heat island, and more frequent heavier rainfall) determined by its complex terrain. To validate the numerical simulations over this coastal region, a combination of conventional surface meteorological observations, radiosondes, and eddy-covariance (EC) measurements collected in July 2020 were utilized.

Conventional surface observations, including 2-m temperature (T), humidity (q), and 10-m wind speed (U) and wind direction (WD), were obtained from four Automatic Weather Stations (AWSs) located in western Shenzhen (marked as S1 to S4 in Fig. 1). These measurements were sampled every 10 min. Turbulence measurements were collected from a tower near Tiegang reservoir in Shenzhen (marked as S5 in Fig. 1), which is close to site S1, with a local altitude of 50.3 m above mean sea level. A three-dimensional (3D) sonic anemometer (CSAT3A, Campbell Scientific Inc., USA) was used to measure 3D wind velocity (u, v, and w) and sonic temperature (T). The CO_2/H_2O Open-Path Gas Analyzer (EC150, Campbell Scientific Inc., USA) was applied to measure

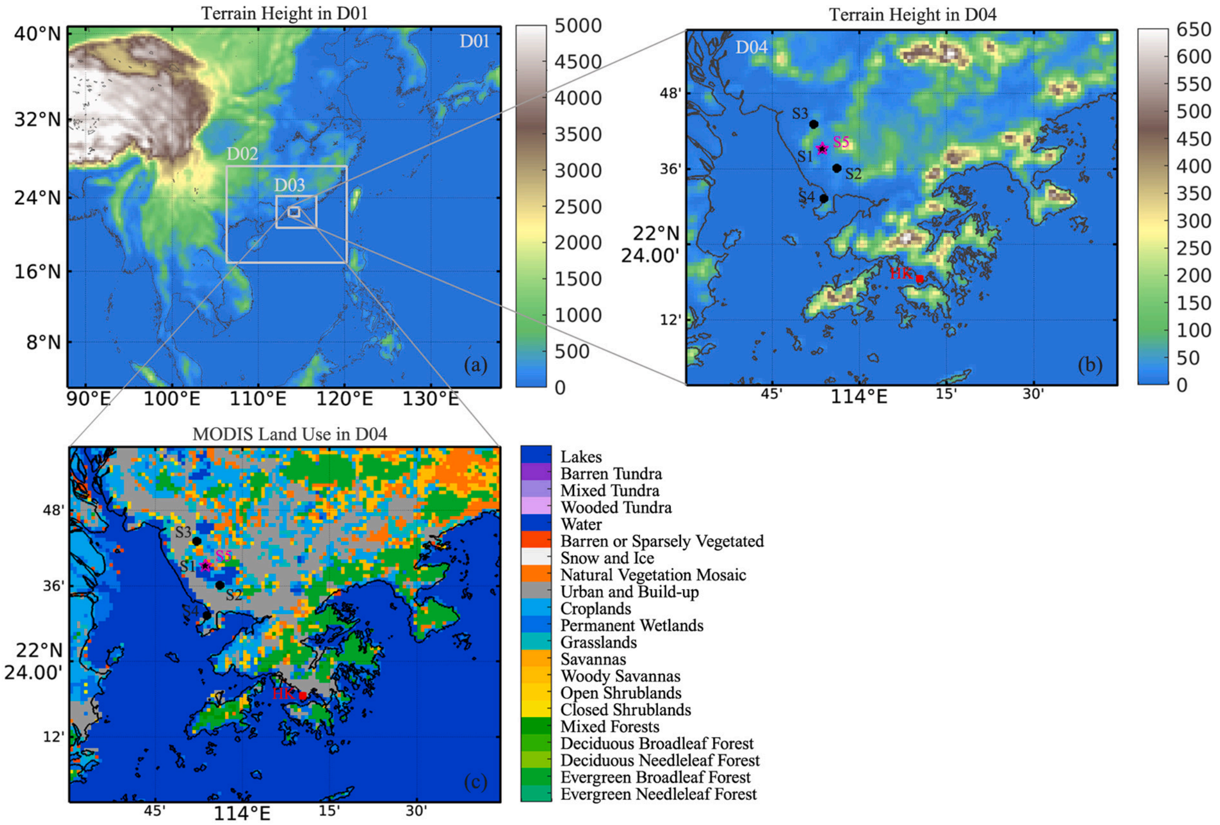

Fig. 1. WRF-nested simulation domains with terrain height for (a) D01 and (b) D04, as well as (c) MODIS land cover type in D04. The black dots denote the locations of AWS sites (S1–S4), the magenta pentagram marks the EC measurement site (S5), and the red square is the GPS-sounding site of Hong Kong King's Park (HK). (For interpretation of the references to colour in this figure legend, the reader is referred to the web version of this article.)

high-frequency water vapor density, carbon dioxide, and barometric pressure. All fast-response sensors were mounted at 10 m above ground level, with a 10 Hz sampling rate. Turbulence statistics, including sensible (*SHF*) and latent (*LHF*) heat fluxes and friction velocity (u_*), were calculated from the fluctuations with 10-min temporal averaging based on the eddy-covariance theory (Kaimal and Finnigan, 1994; Aubinet et al., 2012). Before calculating the turbulent parameters, strict data quality control processing was conducted, such as removing abnormalities, filtering noise, and testing the dimensionless variance similarity (e.g., Kaimal and Finnigan, 1994; Bian et al., 2012). Additionally, the triple coordinate rotation method (Kaimal and Finnigan, 1994) was applied to eliminate the impacts of tilt of the sonic anemometer or terrain on the observation.

In addition, radiosonde measurements from King's Park station (22.311°N, 114.172°E; marked as HK in Fig. 1) in Hong Kong were obtained from the University of Wyoming database (`http://weather.uwyo.edu/upperair/sounding.html;` last access: 15 Jun 2023) and used to validate the simulated vertical tropospheric structures. The GPS sounding measured temperature, humidity, wind speed, and wind direction twice a day at UTC times 00:00 and 12:00, which correspond to the Local Standard Time (LST) of 08:00 and 20:00.

2.2. WRF model configurations

The WRF model version 4.2.1 with ARW (Advanced Research WRF) core (Skamarock et al., 2019) was used in this study. The model was configured with four two-way nested domains with horizontal resolutions of $\Delta x = 27$ km, 9 km, 3 km, and 1 km (Fig. 1). To more accurately simulate the synoptic processes in the southern coastal regions of China, the outermost domain D01 was designed to cover a large region that included part of the Tibetan Plateau and the whole South China Sea with an area of approximately 19800×16500 km^2 (see Fig. 1a). The numbers of the grid points in the zonal and meridional directions for D01–D04 were 181×151, 151×121, 151×121, and 121×100, respectively. The vertical layers were set to 62 levels for all domains with a constant interval of $\Delta z = 50$ m within the lowest 2 km. Above this height, the vertical spacing increased gradually to the model top of 50 hPa, with a 5 km Rayleigh damping layer to prevent contamination by unphysical wave reflections from the upper domain boundary.

The topography data were provided by the Global Multi-Resolution Terrain Elevation Data 2010 30 arcsecs (~ 900 m) dataset (GMTED2010_30s) developed by the U.S. Geological Survey (USGS) (Danielson and Gesch, 2011). The land use data were obtained from Moderate Resolution Imaging Spectroradiometer (MODIS) 20-class land use categories with lakes with the resolution of 15 arcsecs (~ 500 m) (Friedl et al., 2010), as shown in Fig. 1c.

The simulations were initiated every seven days, starting from 00:00 UTC on 30 June 2020. A 31-day simulation was formed by combining data from five simulation trials, with the first 24 h considered as spin-up time in each trial. The initial and lateral boundary conditions (LBCs) were forced by the fifth generation reanalysis datasets ERA5 (Hersbach et al., 2018a, 2018b) of the European Centre for Medium-Range Weather Forecasts (ECMWF), with a spatial resolution of $0.25^\circ \times 0.25^\circ$. The LBCs and sea surface temperature (SST) were updated every 2 h. To ensure numerical stability for the region with complex terrain, an adaptive time step was employed, with a maximum (minimum) time step of 90 s (10 s) for D01. The output was saved at 1 h intervals for D01–D03, and 10 min intervals for D04. For convenience, these mesoscale simulations were labeled MESO27, MESO9, MESO3, and MESO1 based on the grid spacing.

The model physics options included the single-moment 6-class scheme (WSM6; Hong and Lim, 2006) for microphysics parameterization, the rapid radiative transfer model (RRTMG; Iacono et al., 2008) for both shortwave radiation and longwave radiation, the unified Noah model (Chen and Dudhia, 2001) for land-surface parameterization, and the new Tiedtke scheme (Tiedtke, 1989; Zhang et al., 2011) for cumulus parameterization.

To perform sensitivity experiments in the WRF modeling of the PBL over complex terrain, two different PBL schemes were employed: the local closure Mellor-Yamada-Janjić (MYJ; Mellor and Yamada, 1982; Janjić, 1994, 2002) scheme, tied to the Eta surface-layer scheme (Monin and Obukhov, 1954; Janjić, 1994, 2002); and the nonlocal closure Yonsei University (YSU; Hong et al., 2006) scheme, combined with the revised MM5 surface-layer scheme (Jiménez et al., 2012). These two schemes were chosen due to their common usage and ability to provide different representations of PBL turbulence and mixing processes.

2.2.1. MYJ PBL scheme

The MYJ scheme is a 1.5-order local turbulence scheme (Janjić, 1994, 2002) that determines the eddy diffusion coefficient based on the additional prognostic TKE equation, also known as the TKE turbulence scheme. In the local approach, the SGS turbulent fluxes of any adiabatic conserved quantity are assumed to be only related to the gradients of their mean values at adjacent levels. The vertical turbulent diffusion equation can be expressed as

$$\frac{\partial C}{\partial t} = -\frac{\partial}{\partial z}\overline{w'c'} = \frac{\partial}{\partial z}\left[K_c\left(\frac{\partial C}{\partial z}\right)\right] \tag{1}$$

where w' is vertical velocity fluctuation, c' represents the fluctuation of the prognostic variable C (e.g., u, v, θ, and q), $\overline{w'C'}$ is the averaged turbulent fluxes for variable C, and K_c is the eddy diffusivity coefficient for variable C. K_c is proportional to TKE (e), mixing length (l), and stability function (S_c), as described by the equation:

$$K_c = l\sqrt{e}S_c \tag{2}$$

The difference among local schemes lies in how they define and calculate l, S_c, and e. The local scheme is based on local eddy diffusivity for all vertical levels and does not treat the turbulence characteristics within and above the PBL separately, which reduces the spin-up time for the model. The PBL height (PBLH) in this scheme is defined as the height where TKE decreases to a threshold value of 0.1 $m^2\ s^{-2}$.

The MYJ scheme generally shows a cooler, moister, and lower PBL height than other PBL schemes because it does not consider the nonlocal effects and has less entrainment of free-tropospheric air into the PBL (Hu et al., 2010). Despite this limitation, it is still widely used because it is a higher-order scheme that is expected to capture more physics than first-order schemes.

2.2.2. YSU PBL scheme

The YSU scheme is a first-order nonlocal turbulence closure that considers the entrainment process and follows a parabolic K-theory. For the mixed layer, the YSU scheme adds two more terms (nonlocal gradient adjustment and entrainment flux) than the local scheme to express the turbulent diffusion (Hong et al., 2006), as described by the equation:

$$\frac{\partial C}{\partial t} = -\frac{\partial}{\partial z}\overline{w'c'} = \frac{\partial}{\partial z}\left[K_c\left(\frac{\partial C}{\partial z} - \gamma_c\right) - \overline{(w'c')_h}\left(\frac{z}{h}\right)^3\right] \tag{3}$$

where h is the diagnosed PBLH determined by the critical bulk Richardson number method (e.g., Seibert et al., 2000), and $\overline{(w'c')}_h$ is the flux at the inversion layer. The counter-gradient mixing term γ_c represents the contribution of the large-scale eddies to the total flux, and it is only applied to potential temperature and horizontal velocity components, but not to passive variables (e.g., q) since they are not necessarily correlated with the thermals (Hong et al., 2006). The primary effect of γ_c is to neutralize the temperature gradient (and wind shear) by raising the temperature (decreasing wind speed) in the upper part and lowering (increasing) it in the lower part of the PBL (Hong et al., 2006). The last term $-\overline{(w'c')}_h\left(\frac{z}{h}\right)^3$ represents the explicit parameterization of the entrainment flux at the top of the PBL, which is the most critical step in improving the representation of the convective boundary layer (CBL) and only works within the PBL (Hong et al., 2006; Milovac et al., 2016).

Compared to the local scheme, the YSU scheme typically produces warmer, drier, and deeper daytime PBLs due to its consideration of nonlocal transport, resulting in enhanced vertical mixing and entrainment (Hu et al., 2010). It may be more suitable for modeling SGS exchange over complex topography due to its consideration of counter-gradient correction or additional mixing (e.g., Serafin et al., 2018). However, this scheme is highly sensitive to the diagnosed PBLH (Milovac et al., 2016), which can be difficult to estimate accurately. This sensitivity can affect the accuracy of the scheme, as errors in the PBLH estimation can be propagated to the calculation of the nonlocal gradient adjustment and the entrainment flux terms, potentially leading to errors in the predicted PBL structure and evolution.

3. Results

3.1. Near-surface variables

3.1.1. Diurnal variation

To evaluate the performance of WRF simulations with different PBL schemes at varying horizontal resolutions, a statistical analysis was performed on the average of each first-order variable across all sites (as shown in Table 1) and each second-order variable at site S5 (see Table 2) during the entire month of July 2020. The mean bias (MB), root mean square error (RMSE), and correlation coefficient (R) between simulations and observations were calculated for the whole day (marked as "All"), for only daytime (06:00–18:00 LST, marked as "Daytime"), and for only nighttime (18:00–06:00 LST, marked as "Nighttime"), as shown in Table 1 and Table 2. Additionally, we present the mean diurnal variations of near-surface variables during July 2020 in Fig. 2. Since the observation sites are located close to each other within a distance of 22 km, we did not analyze the simulations of MESO27 in this study.

Fig. 2 shows clear diurnal variations in all observed near-surface first- and second-order variables. For instance, the near-surface heat fluxes (*SHF* and *LHF*) increase rapidly after sunrise (06:00 LST) and reach their maximum at noon (12:00 LST), about 2 h before the 2-m T peak. This lag occurs because direct ground heating by solar radiation does not immediately warm the surface and near-surface air due to the high land surface heat capacity. As the sun sets, upward longwave radiation dominates the surface energy balance, cooling the surface and leading 2-m T to drop continuously and reach its minimum ($\sim$ 28 °C) in the early morning (05:00 LST). This diurnal cycle is typical for summer air temperature in tropical coastal regions, featuring a moderate fluctuation of around 5 °C throughout the entire day and relatively small changes of <1 °C during the nighttime. This pattern can be attributed to the moderate daytime *SHF* (average of 63.7 ± 55.8 W m^{-2}) and the small nighttime *SHF* (average of -6 ± 4.9 W m^{-2}), as shown in Fig. 2 and Table 2. The wind speed and friction velocity also exhibit a similar diurnal cycle as T, with peaks usually $1 \sim 2$ h after T due to downward momentum flux transport from thermal effects.

The comparisons show that while the mesoscale WRF simulations face challenges in accurately reproducing the diurnal amplitudes for some variables (e.g., U and turbulent fluxes), they are able to adequately capture the observed diurnal cycles for all near-surface meteorological variables (see Fig. 2). This indicates that the model can effectively simulate the physical processes responsible for the diurnal cycle. In our cases, the simulated 2-m T from all sets of runs are lower than the observed T overall, with a mean bias ranging from $-0.46 \sim -0.19$ °C depending on the model resolution and PBL schemes. Such colder biases for both MYJ and YSU schemes are consistent with previous studies by

Table 1

Comparison of the statistics for near-surface first-order parameters between WRF simulations and observations based on the averages of the sites S1–S4 during July 2020, with a time interval of 1 h. The variables include air temperature at 2-m height (2-m *T*; °C) and wind speed (10-m *U*; m s^{-1}) and direction (10-m *WD*; °) at 10-m height. The means and standard deviations of the observations are shown in parentheses. MB, RMSE, and R represent mean bias (simulation − observation), root mean square error, and correlation coefficient between simulation and observation, respectively.

			MESO9		MESO3		MESO1	
			MYJ	YSU	MYJ	YSU	MYJ	YSU
All	2-m *T* (30.14 ± 2.05)	MB	−0.35	−0.46	−0.19	−0.26	−0.21	−0.37
		RMSE	0.86	1.00	0.87	0.93	0.88	0.91
		R	0.924	0.907	0.912	0.911	0.917	0.915
	10-m *U* (2.19 ± 1.11)	MB	2.90	2.59	2.98	2.61	2.90	2.43
		RMSE	3.35	3.05	3.40	3.04	3.30	2.89
		R	0.650	0.680	0.691	0.690	0.685	0.726
	10-m *WD* (178.0 ± 46.9)	MB	9.4	13.5	7.7	12.9	7.8	12.6
		RMSE	41.9	38.8	43.0	39.9	40.2	39.2
		R	0.541	0.634	0.521	0.609	0.566	0.618
Daytime 06:00–18:00 LST	10-m *T* (31.43 ± 2.08)	MB	−0.39	−0.70	−0.32	−0.59	0.03	−0.41
		RMSE	0.96	1.18	1.05	1.12	1.02	1.07
		R	0.909	0.898	0.876	0.888	0.882	0.884
	10-m *U* (2.56 ± 1.14)	MB	3.00	2.67	3.02	2.56	2.99	2.66
		RMSE	3.48	3.25	3.49	3.11	3.40	3.18
		R	0.703	0.706	0.744	0.727	0.745	0.745
	10-m *WD* (188.8 ± 45.3)	MB	9.5	13.6	6.6	12.7	6.5	11.7
		RMSE	44.7	40.6	45.6	42.6	40.7	40.9
		R	0.462	0.570	0.466	0.547	0.531	0.559
Nighttime 18:00–06:00 LST	2-m *T* (28.99 ± 1.15)	MB	−0.30	−0.24	−0.06	0.04	−0.43	−0.33
		RMSE	0.77	0.80	0.66	0.69	0.74	0.75
		R	0.786	0.749	0.818	0.800	0.849	0.826
	10-m *U* (1.86 ± 0.96)	MB	2.82	2.53	2.94	2.65	2.82	2.22
		RMSE	3.22	2.85	3.31	2.98	3.22	2.61
		R	0.535	0.611	0.596	0.633	0.572	0.649
	10-m *WD* (168.4 ± 46.2)	MB	9.3	13.5	8.7	13.1	8.9	13.4
		RMSE	39.2	37.2	40.5	37.4	39.8	37.6
		R	0.573	0.665	0.537	0.653	0.554	0.651

Table 2

Same as Table 1, but for the second-order variables of surface sensible heat flux (*SHF*; W m^{-2}), latent heat flux (*LHF*; W m^{-2}), and friction velocity (u_*; m s^{-1}) at the EC site S5.

			MESO9		MESO3		MESO1	
			MYJ	YSU	MYJ	YSU	MYJ	YSU
All	*SHF* (27.0 ± 51.9)	MB	134.8	128.2	42.8	39.2	54.4	49.0
		RMSE	217.0	203.0	92.0	77.4	106.9	89.9
		R	0.868	0.857	0.876	0.874	0.883	0.879
	LHF (46.5 ± 58.6)	MB	−22.6	−22.8	69.1	69.3	55.9	55.8
		RMSE	55.0	56.3	118.1	120.9	96.3	97.6
		R	0.515	0.521	0.829	0.803	0.825	0.812
	u_* (0.21 ± 0.11)	MB	0.44	0.44	0.29	0.25	0.31	0.26
		RMSE	0.49	0.50	0.34	0.32	0.36	0.33
		R	0.526	0.540	0.561	0.578	0.553	0.580
Daytime LST 06:00–18:00	*SHF* (63.7 ± 55.8)	MB	270.7	251.0	106.8	89.8	129.1	108.4
		RMSE	312.4	291.6	132.2	111.8	154.1	130.1
		R	0.750	0.728	0.759	0.752	0.773	0.763
	LHF (88.7 ± 61.5)	MB	−47.6	−47.8	143.8	143.6	115.7	115.2
		RMSE	79.2	80.9	170.3	174.3	138.6	140.7
		R	0.228	0.253	0.652	0.607	0.644	0.623
	u_* (0.27 ± 0.12)	MB	0.46	0.47	0.32	0.29	0.34	0.32
		RMSE	0.51	0.54	0.37	0.36	0.39	0.38
		R	0.403	0.414	0.428	0.429	0.414	0.416
Nighttime LST 18:00–06:00	*SHF* (−6.0 ± 4.9)	MB	12.9	18.1	−14.5	−6.3	−12.6	−4.3
		RMSE	42.0	43.3	19.5	12.5	18.8	12.6
		R	0.509	0.517	0.538	0.582	0.536	0.560
	LHF (8.7 ± 9.8)	MB	−0.1	−0.4	2.1	2.7	2.3	2.6
		RMSE	11.0	11.3	21.5	22.1	18.6	18.5
		R	0.344	0.406	0.510	0.522	0.507	0.532
	u_* (0.16 ± 0.07)	MB	0.42	0.41	0.27	0.21	0.29	0.21
		RMSE	0.47	0.46	0.32	0.27	0.33	0.27
		R	0.548	0.527	0.544	0.521	0.537	0.520

Hu et al. (2010) and Zhang et al. (2012) in urban sites. Compared to MYJ runs, the temperatures predicted with YSU runs are about 0.2 ∼ 0.3 °C lower during the daytime and around 0.1 °C warmer at nighttime. This inconsistency between day and night is most likely related to the stronger turbulent mixing in YSU runs, which quickly mixes the energy transported from the surface (heating during the day and cooling at night) and entrained from the PBL top more homogeneously within the PBL than the local scheme. Overall, MYJ runs predict 2-m *T* more

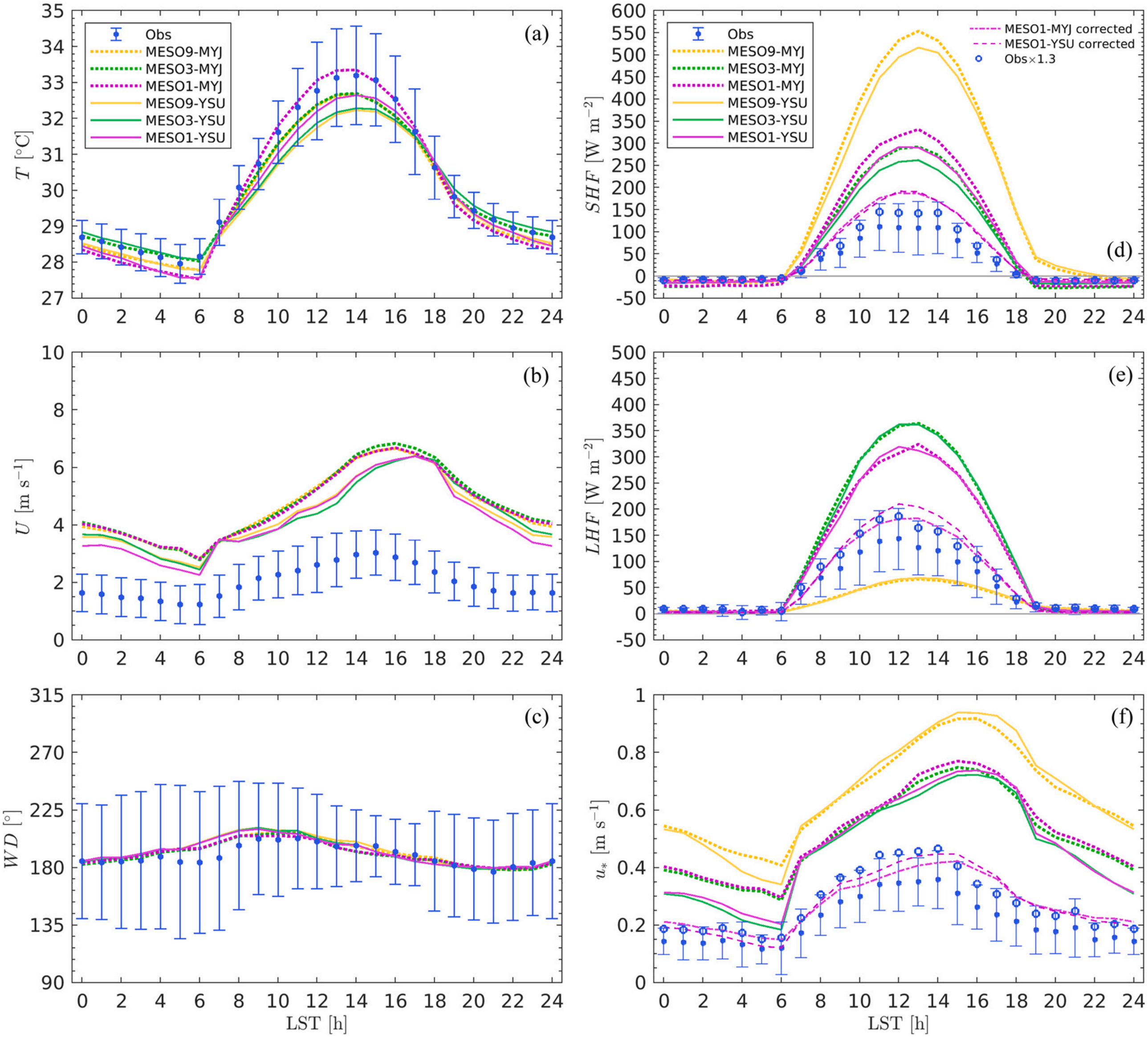

Fig. 2. Mean diurnal variations of the near-surface meteorological variables throughout the 1-month simulation period. (a–c) 2-m temperature (T), 10-m wind speed (U) and wind direction (WD) averaged from AWS sites S1–S4. (d–f) Surface sensible heat flux (SHF), latent heat flux (LHF), and friction velocity (u_*) at the EC site S5. For clarity, only the standard deviation of the observation is shown in the figure. In (d–f), the magenta dash-dotted and dashed lines are the corrected turbulent fluxes based on the observed near-surface wind speed for the two PBL schemes at 1 km resolution respectively. The corrected flux F_C is obtained from the following equation: $F_c = F \times U_{obs}/U_{sim}$, where U_{obs} and U_{sim} are observed and simulated 10-m wind speed, and F is simulated flux (i.e., SHF, LHF, and u_*). The blue cycles indicate the observations increased by 30% according to the worst energy closure of EC measurements over crops (Stoy et al., 2013). (For interpretation of the references to colour in this figure legend, the reader is referred to the web version of this article.)

accurately during the daytime, while it is the opposite during nighttime in our cases, and this conclusion is independent of the model resolution (as shown in Table 1 and Fig. 2).

For near-surface winds, the WRF model reproduces the observed southerly winds very well (the MB of WD around 10° and R in the range of $0.55 \sim 0.65$) during the entire day for all resolutions (MESO9, MESO3, and MESO1). However, it systematically overestimates U by about $2 \sim 3$ m s^{-1} with both local and nonlocal PBL schemes. The U biases are almost equivalent to or slightly larger than the observed U, with the values in the range of $2.6 \sim 3.5$ m s^{-1}. The systematic overestimation of 10-m U and the underestimation of 2-m T in both MYJ and YSU schemes (see Fig. 2) are possibly due to the coarse-resolution of the land-use data used in the WRF model, which cannot accurately describe the actual urban features and distribution in a city like Shenzhen with complex terrain. Additionally, the urban canopy model is not utilized in the simulations, which can also contribute to the discrepancies between the simulations and observations. Compared to MYJ runs, the wind speeds predicted by YSU runs under all different resolutions are more consistent with observation over the entire day, with the values of MB and RMSE about $0.3 \sim 0.5$ m s^{-1} smaller than those for MYJ runs and a relatively larger R (especially during nighttime), as shown in Table 1. YSU runs also reproduce more accurate diurnal variation of wind direction than that from MYJ runs, despite the fact that its MB is usually 4° larger than that of MYJ runs.

For surface turbulent parameters, the MESO9 simulations show much larger biases than the other runs. Since the land-use category at the location of the S5 site in D02 is urban, which is inconsistent with the farmland underlying surface of the observation site, resulting in an obviously larger SHF and smaller LHF during the daytime, as well as larger u_* throughout the entire day (see Fig. 2d–e). Therefore, we exclude the simulated turbulent parameters from MESO9 in the following comparisons. The WRF model significantly overestimates *SHF*, *LHF*, and u_* with both MYJ and YSU schemes at all different horizontal resolutions. During the daytime, the simulated *SHF*, *LHF*, and u_* with both MYJ and YSU schemes can reach around 300 W m^{-2}, 350 W m^{-2} and 0.75 m s^{-1}, respectively. These values are about 2 ~ 3 times greater than the corresponding observed values, resulting in large daytime MBs. This apparent overestimation of near-surface turbulent fluxes by the WRF model is also reported in Sun et al. (2017) and Sathyanadh et al. (2017), in which they mainly attributed it to the surface layer parameterization scheme and the accuracy of the land-use data. During the nighttime, the WRF model reproduces the downward sensible heat flux transfer process (i.e., negative *SHF*), but it transfers more energy to the surface with an MB of approximately 1 ~ 2 times of the observation (-6.0 ± 4.9 W m^{-2}). The simulated nighttime *LHF* is about 24 ~ 30% (i.e., 2.1 ~ 2.7 W m^{-2}) larger than the observed value (8.7 ± 9.8 W m^{-2}). Additionally, the WRF model tends to overestimate the nighttime u_*, with an MB ranging from 1.3 to 1.8 times the observed value of 0.16 ± 0.07 m s^{-1}. This apparent overestimation of near-surface turbulent fluxes (i.e., *SHF*, *LHF*, and u_*) throughout the whole day (including the notably negative nighttime *SHF*) by the WRF model is likely to be caused by the overestimated wind speeds throughout the entire day or/and the underestimation of observed fluxes by EC methods. To verify this, we corrected the simulated fluxes using the observed wind speed (see the magenta dash-dotted and dashed lines in Fig. 2d–f) and increased the observed fluxes by 30% (see blue cycles in Fig. 2d–f) based on the worst average closure (0.70 ~ 0.78) of EC measurements over crops (Stoy et al., 2013). The agreement between simulations and observations gets better after the corrections and the overestimated wind speed is the primary factor leading to the overestimation of near-surface turbulent fluxes.

The comparison of the two PBL schemes reveals that YSU runs generally yield more accurate *SHF* throughout the entire day, with the absolute value of MB and RMSE smaller than those of the MYJ scheme. This explains why the 2-m *T* simulated by YSU is colder during daytime and slightly warmer during nighttime than that of MYJ runs in Fig. 2 and Table 1. The fact that the daytime *SHF* predicted by YSU is lower than that of MYJ is also often reported in the literature, such as Fig. 6 in Zhang et al. (2012), Fig. 5a in Hu et al. (2010), and Fig. 6a in Sathyanadh et al. (2017), which is likely related to the different surface layer schemes paired with MYJ and YSU PBL parameterizations. The *LHF* predicted by MYJ and YSU runs is consistent throughout the whole day, with small differences of <0.5 W m^{-2}. Additionally, the u_* predicted by YSU runs is closer to the observations than that of MYJ over the entire day, resulting in more accurate simulated *U*.

We also evaluate the model performance with varying horizontal resolutions from 1 to 9 km. During the daytime, the model exhibits superior performance at 1 km resolution for all near-surface variables, as indicated by the relatively higher R and smaller MB and RMSE in Table 1–2, except for *SHF* and u_* (where MESO3 outperforms). For instance, when the horizontal resolution increases from 9 km to 1 km, the absolute MBs of *T* (*LHF*) for both PBL schemes are reduced by >0.3 °C (30 W m^{-2}). During the nighttime, MESO3 performs better for *T*, while MESO1 outperforms for winds (*U* and *WD*) and *SHF*. For *LHF* and u_*, both MESO1 and MESO3 yield similar results with differences smaller than 0.2 W m^{-2} and 0.02 m s^{-1}, respectively. For the entire day, MESO3 produces the most accurate *T*, *SHF*, and u_*, while MESO1 performs best in other variables, especially winds and *LHF* (refer to Fig. 2 and Table 1–2). These findings suggest that increasing the horizontal resolution can generally improve the model's performance, especially for winds and daytime temperature, although the degree of improvement depends on the variables and time periods.

3.1.2. Simulation errors analysis

The analysis in Section 3.1.1 reveals that the simulation error of each variable has a clear diurnal variation (also see Fig. A1). Therefore, it is necessary to evaluate the WRF simulation skills for each near-surface variable at different conditions.

Fig. 3 displays the distribution of simulation biases at all observation sites as a function of observed values, and the probability density function (PDF) of simulation errors for each near-surface variable. For the temperature, the simulated error slightly decreases with the increase of observed *T* when $T < 28$ °C and remains almost constant at about −0.2 °C for 28°C< $T < 31$ °C. Then, the negative deviation increases with the increase of observed *T* when $T > 31$ °C. Such an apparent cold bias in the model at high temperatures occurs mostly in sunny afternoons, mainly because the land-use data and urban parameters in the model do not describe the real underlying surface of the metropolitan region. The comparison of the two schemes shows that they are almost identical when $T < 31$ °C, while the YSU scheme yields a relatively colder bias than MYJ when $T > 31$ °C, but it is not as dispersed as that of MYJ runs. The difference between the two schemes is most pronounced during the daytime, with the PDF peak of YSU bias shifted by about 0.5 °C to the left of MYJ (Fig. 3e).

The bins-averaged bias of wind speed does not change significantly (around 2.5 ~ 3 m s^{-1}) with the increase of observed *U* (when $U > 1$ m s^{-1}) for both MYJ and YSU schemes, while the bias distribution is more scattered when $U < 4$ m s^{-1}, which is also reported by Zhang et al. (2012). Notably, <1% of the dots are below the zero line in Fig. 3b, which again demonstrates the systematic overestimation of near-surface wind speeds by the WRF model over complex terrain. The *U* bias for YSU is smaller than that for MYJ during both daytime and nighttime (Fig. 3f), showing that YSU runs reproduce more accurate wind speed than MYJ runs throughout the whole day.

For *SHF* and *LHF*, the errors for both YSU and MYJ almost linearly decrease as observations increase when the observed values are <0 W m^{-2}. When the observed *SHF* (*LHF*) > 0 W m^{-2}, the errors initially rapidly increase with increased observed values and then gradually decrease when the observed *SHF* (*LHF*) > 100 W m^{-2} (Fig. 3c, d). Moreover, they are mainly concentrated within ±10 W m^{-2} at night, while they are widely distributed from −20 to 300 W m^{-2} during the daytime (see Fig. 3g, h). The YSU scheme obtains smaller errors in *SHF*, especially when the observed *SHF* ≥ 20 W m^{-2}. The comparison shows that there is no significant difference in the latent heat errors yielded by MYJ and YSU schemes, both in the PDF distribution and its trend with the observed values.

The simulation errors display significant uncertainties (with a large dispersion shown in Fig. 3c,d) when observed heat fluxes are less than approximately 150 W m^{-2}. These large uncertainties implicate that simulating surface turbulent fluxes with mesoscale models remains a formidable challenge. This difficulty is primarily due to three factors: (1) the land cover dataset used in the WRF model significantly differs from the actual LC; (2) the default configuration of the model ignores the variability of LC in the subgrid and uses only the dominant LC category in each pixel as surface information (known as the dominant approach), which would exacerbate the discrepancy between simulated and observed fluxes (Román-Cascón et al., 2021); (3) the potential failure of the flatten, homogeneous and the vertically-constant-flux assumptions in the surface layer, which disregards local advection processes between grid cells resulting from inherent horizontal heterogeneity in complex terrain (Shao et al., 2013; Serafin et al., 2018).

3.2. PBL height and vertical structure

The PBLH is a crucial factor for evaluating model performance, as its accuracy directly impacts the precision of atmospheric chemistry predictions (Misenis and Zhang, 2010). To ensure consistency, we recalculated PBLH for simulations using the bulk Richardson number (Ri_b) method with the same threshold (0.25) to avoid the influence of different diagnostic methods on PBLH in different schemes. This

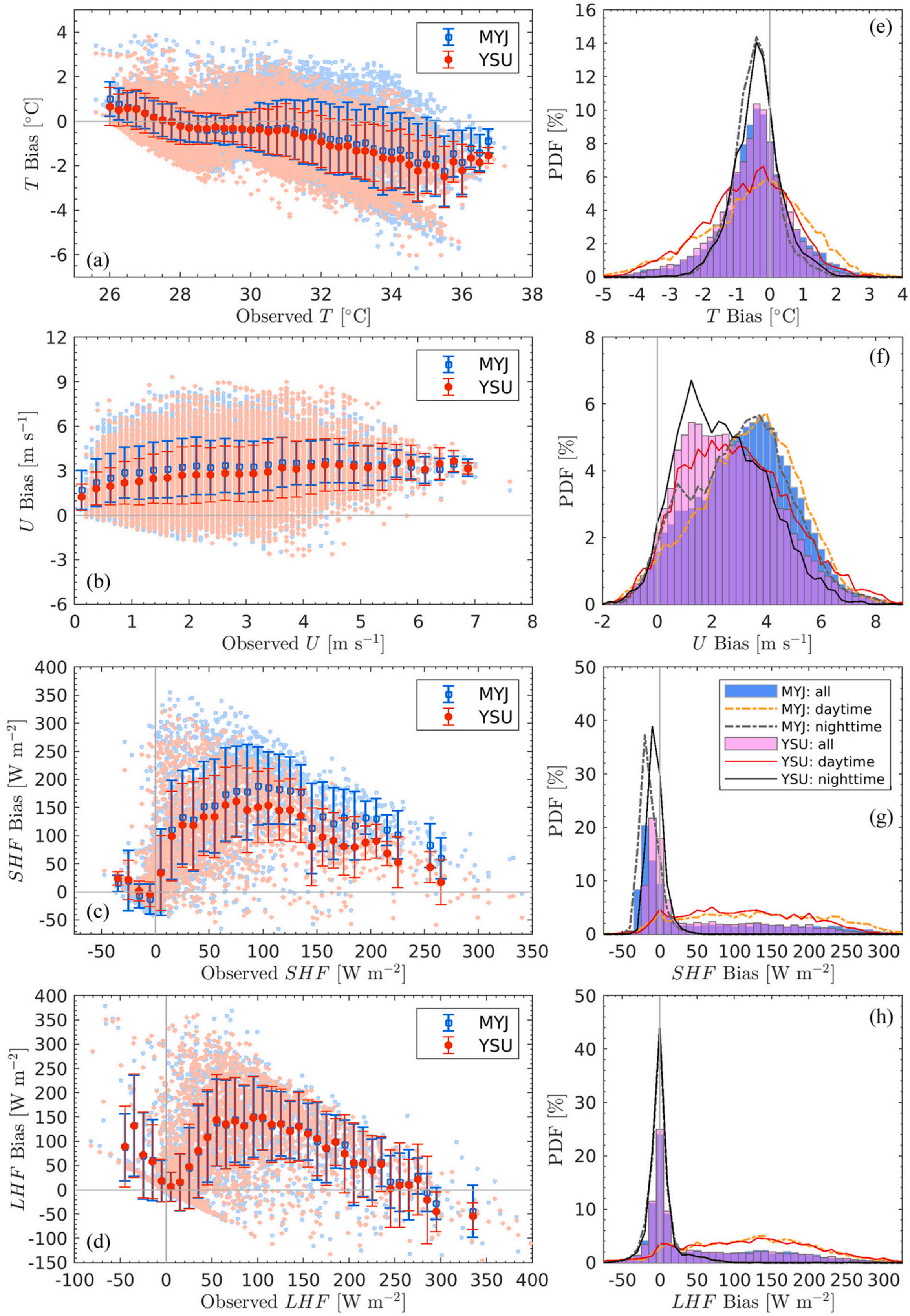

Fig. 3. Simulation biases against the corresponding observations (left panel) and their probability density function (PDF; right panel) during the 1-month simulation period. (a, e) 2-m air temperature (*T*), (b, f) 10-m wind speed (*U*), (c, g) surface sensible heat flux (*SHF*), and (d, h) surface latent heat flux (*LHF*). The simulations are from MESO1 with 10-min time intervals. For *T* and *U*, data from all four sites (S1–S4) are included in the figures. For *SHF* and *LHF*, only the data from EC site S5 is shown. The squares (MYJ) and dots (YSU) with error bars are averages with standard deviations for the bins (0.2 °C for *T*, 0.25 m s^{-1} for *U*, and 10 W m^{-2} for *SHF* and *LHF*).

recalculated PBLH is marked as h_{cal}, while the original model-diagnosed PBLH is marked as h_{omd}. We also applied this method to GPS-sounding profiles.

Fig. 4 compares simulated PBLH from the WRF model (including both h_{omd} and h_{cal}) with observations. The PBLH values diagnosed by both the MYJ and YSU schemes are consistently lower than the observed values. Specifically, the monthly averages of h_{omd} predicted by the MYJ and YSU schemes are 411.1 ± 82.4 m and 564.3 ± 92.4 m, respectively, which are approximately 47.2% and 27.5% lower than the observed value of 778.3 ± 238.2 m. This systematic underestimation of PBLH in both local and nonlocal schemes has also been reported by Banks and Baldasano (2016). Due to the large uncertainties between different diagnostic methods, there is a small correlation between the WRF-diagnosed PBLH (i.e., h_{omd}) and the observations (as shown in Fig. 4b). The comparison reveals that h_{omd} predicted by the MYJ scheme is approximately 25.1% lower than that predicted by the YSU scheme in a monthly average. This finding is consistent with that of Misenis and Zhang (2010), who reported that the PBLH diagnosed by the MYJ scheme was $20 \sim 40\%$ lower than that of the YSU scheme. Such lower PBLH predicted by the local PBL scheme may cause air quality models to produce higher levels of pollutants (such as O_3 and CO) within the PBL (Misenis and Zhang, 2010; Banks and Baldasano, 2016).

When applying the bulk Richardson method with the same threshold value to recalculate the PBLH, the monthly mean values for both the MYJ and YSU schemes, obtained from all 10-min time interval data, are 673.7 ± 165.0 m and 661.9 ± 170.4 m, respectively. These values are close to the diagnosed value (602.0 ± 231.0 m) by YSU and significantly higher than the diagnosis of MYJ (423.2 ± 119.8 m). To compare with observations, the recalculated PBLH is averaged only for the measurement times. The results are almost identical for both PBL schemes (647.6 ± 126.8 m and 645.3 ± 154.0 m, respectively), which are approximately 17% lower than the observed PBLH (h_{obs}). Although h_{cal} still underestimates the observations when $h_{obs} > 900$ m, it exhibits more consistency with the observations, with a statistically significant linear relationship for the MYJ and YSU schemes respectively being $h_{cal} = 0.25h_{obs} + 451.8$ ($R = 0.4404$, $p < 0.001$) and $h_{cal} = 0.27h_{obs} + 422.3$ ($R = 0.4142$, $p < 0.001$), see Fig. 4b. Compared with h_{omd}, we suggest adjusting the threshold values for TKE in the MYJ scheme and Ri_b in the YSU scheme to improve the accuracy of PBLH diagnosis, especially by reducing the TKE threshold value in the MYJ scheme.

The difference in PBLH predicted by the two PBL schemes appears to be mainly caused by their corresponding K_h values (see Fig. 5). The maximum monthly mean K_h values in the PBL for the YSU scheme are 1.9 and 2.8 times higher than those for the MYJ scheme at 08:00 and 20:00 LST, respectively. Such relatively strong local vertical mixing leads to a considerable increase in the PBLH in the nonlocal PBL scheme. There is a discernible connection between h_{omd} and K_h, as demonstrated by the relationships between PBLH and either the maximum K_h within the PBL, $max(K_h(z))$, or the vertical integration of K_h ($\Sigma K_h(z) = \int_0^{z_m} K_h(z)dz$, where z_m is the height at which K_h starts <0.1 m^2 s^{-1}), as shown in Fig. 5b,c. The relationships between h_{omd} and K_h are as follows: $h_{omd} = 2.42max(K_h(z)) + 347.0$ ($R = 0.547$, $p < 0.001$) and $h_{omd} = 189.68log_{10}(\Sigma K_h(z)) - 284.9$ ($R = 0.787$, $p < 0.001$) for the MYJ scheme, and $h_{omd} = 2.38max(K_h(z)) + 414.6$ ($R = 0.695$, $p < 0.001$) and $h_{omd} = 256.34log_{10}(\Sigma K_h(z)) - 555.4$ ($R = 0.755, p < 0.001$) for the YSU scheme.

Fig. 6 displays the monthly mean profiles of simulated and observed potential temperature (θ), specific humidity (q), wind speed (U), and wind direction (WD) at King's Park station at 08:00 and 20:00 LST in July 2020. It is evident that h_{omd} is significantly lower than the observed PBLH (756 m at 08:00 LST and 781 m at 20:00 LST), while h_{cal} is more consistent with the observation, with a monthly MB of $-150 \sim -100$ m. The simulations using both MYJ and YSU schemes generally reproduce well the observed vertical thermodynamic structure of the lower troposphere. However, the model tends to underestimate the air temperature throughout the entire PBL, with a monthly MB of $-0.6 \sim -0.1$ K at 08:00 LST and $-1.0 \sim -0.3$ K at 20:00 LST. The maximum negative bias occurs in the middle of the PBL. This underestimation of air temperature for both local and nonlocal PBL schemes is also found in Hu et al. (2010), indicating the presence of common error sources such as incorrect land use or urban surface properties. Below the PBLH, due to stronger local vertical mixing and additional entrainment processes, the YSU scheme produces a more accurate θ, which is about $0.05 \sim 0.15$ K warmer than that of MYJ, resulting in a relatively higher ($0.2 \sim 0.5$ g kg^{-1}) humidity than the MYJ scheme. This finding contradicts previous studies that have shown nonlocal schemes tend to produce warmer and drier PBLs, while local schemes typically generate colder and moister PBLs (Hong and Pan, 1996; Hu et al., 2010; Xie et al., 2012; Milovac et al., 2016). The observed discrepancy in this study is likely due to the influence of complex terrain and land-sea interactions. Additionally, the entrainment mixing effect is conducive to raising the height of PBL and warming it, rather than reducing the water vapor within the PBL, since the humidity difference between the free atmosphere and the PBL top region is relatively small in coastal areas (Ma et al., 2018). Therefore, the YSU scheme produces warmer and moister PBL compared to the MYJ scheme in the coastal regions.

Both the MYJ and YSU schemes significantly overestimate U within the PBL, especially near the surface, with a monthly MB of ~ 4 m s^{-1} at 08:00 LST and ~ 5 m s^{-1} at 20:00 LST. Both PBL schemes generate an apparent low-level jet around $200 \sim 400$ m in the evening, which is not observed in actual measurements. This discrepancy can primarily be attributed to uncertainties in interpolation caused by the limited number

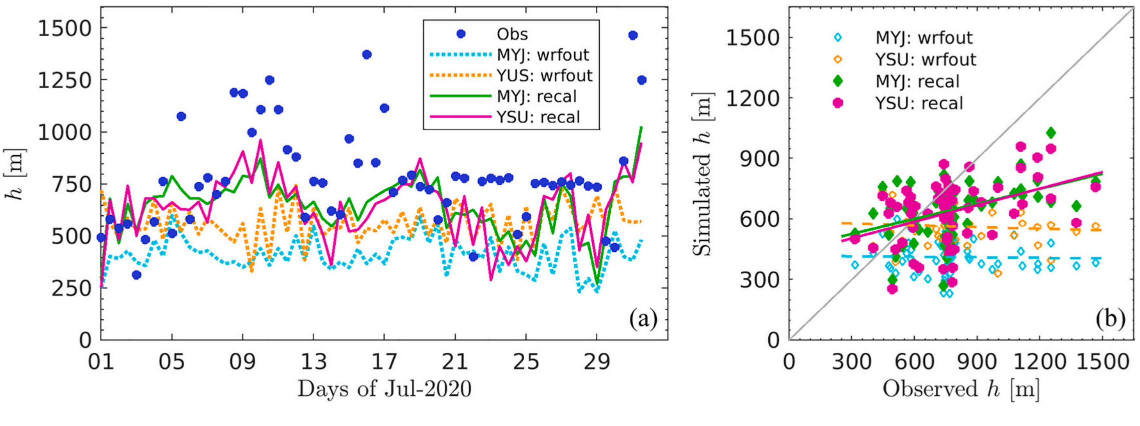

Fig. 4. (a) Observed and simulated PBLH (h) at Hong Kong King's Park station in July 2020. (b) Relationship between simulated and observed h. The original model-diagnosed PBLH from WRF output is tagged with "wrfout", and the value recalculated using the Richardson number method is labeled "recal". Observations and MESO1 simulations are sampled at 08:00 and 20:00 LST each day.

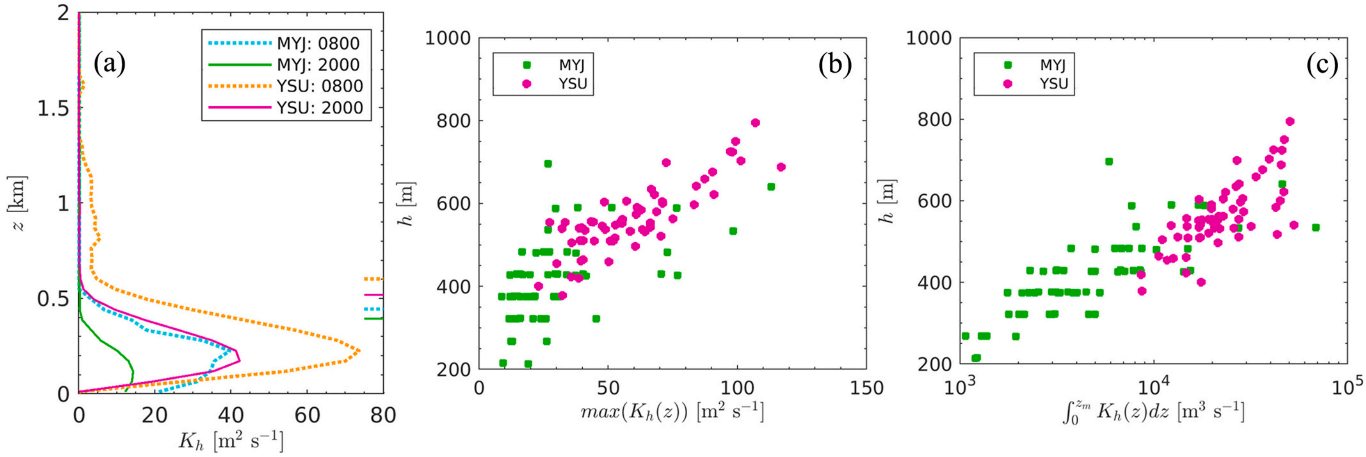

Fig. 5. (a) Monthly mean eddy diffusivity for thermal properties (K_h; m^2 s^{-1}) calculated with the MYJ and YSU PBL schemes at 08:00 and 20:00 LST at Hong Kong King's Park station during July 2020. The PBLH (h_{omd}) is marked on the figure with short horizontal lines. (b–c) The relationships between simulated PBLH (h_{omd}) and (b) maximum K_h within the PBL, as well as (c) the vertical integration of K_h ($\int_0^{z_m} K_h(z)dz = \Sigma K_h(z)$; m^3 s^{-1}).

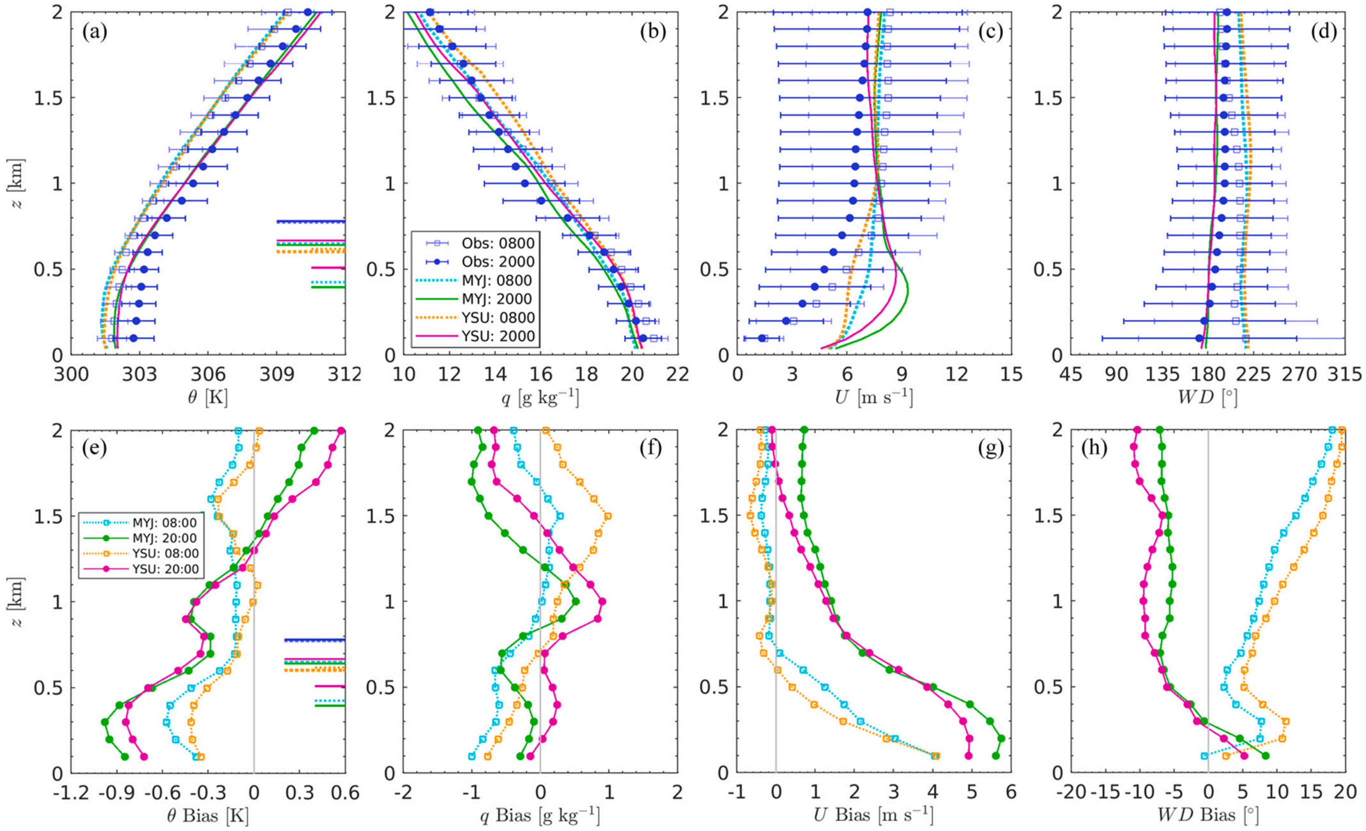

Fig. 6. Monthly mean vertical profiles of (a) potential temperature (θ), (b) specific humidity (q), (c) wind speed (U), and (d) wind direction (WD) at 08:00 and 20:00 LST at Hong Kong King's Park station during July 2020. (e-h) Monthly mean biases between simulations and observations for the corresponding variables. The simulations are from MESO1. Error bars in (a–e) represent the standard deviations of observations. The horizontal bars in (a, e) denote the PBLH for the corresponding profiles, where short bars indicate the model-diagnosed PBLH and long bars are the recalculated PBLH.

of valid near-surface measurements, as well as the omission of building morphology effects in the model. The overestimation of wind speed decreases rapidly with altitude. Above the PBLH, the simulations agree well with the observations, with an absolute MB of <1 m s^{-1}. These findings suggest that urban canopy parameterizations should be applied when simulating the urban atmospheric environment, especially in high-density built-up regions. Regarding the wind direction, both PBL schemes accurately reproduce the observed *WD* in the lower troposphere, as indicated by monthly absolute MB typically around 5° within the PBL and ~ 10° above the PBL. In addition, the comparison indicates that overall, the YSU produces more accurate wind fields than the MYJ scheme throughout the entire PBL, for both morning and evening hours.

3.3. Effect of land cover

The study area of interest, as depicted in Section 2.1 and Fig. 1b, is surrounded by seas except for the north, with land and sea grid points accounting for about 48.1% and 50.5% of the total grids in the domain D04, respectively, and the remaining 1.4% being lakes. The distinct surface properties of land and sea, such as albedo, thermal conductivity, heat capacity, and roughness, have a direct impact on the surface energy balance, leading to different PBL structures over the two surfaces, as evidenced by the markedly different diurnal variations of near-surface meteorological variables for land and sea, as shown in Fig. A2. Therefore, it is essential to examine the performance of PBL schemes over land and sea, for which we perform a statistical analysis of the average of each variable across all terrestrial and oceanic grid points of the domain D04.

3.3.1. Near-surface variables over the land and sea

As shown in Fig. 7, the mean diurnal variations of differences between the YSU and MYJ schemes (Δ = YSU − MYJ) for near-surface variables reveal considerable deviations between these two schemes over the land and sea, even though they obtain a similar mean diurnal variation of each variable over the land and sea (see Fig. A2). Except for surface *LHF* and *q*, which are more influenced by the water surface, the differences between the YSU and MYJ schemes for all near-surface variables are significantly larger over the land than those over the sea. For instance, over the sea, the diurnal amplitudes of ΔT_2, ΔSHF, and Δu_* are approximately 0.2 °C, 2 W m^{-2}, and 0.03 m s^{-1} respectively, while over the land these values increase several times with relatively high variability (as shown by the larger standard deviation in Fig. 7). Over the land, the YSU scheme predicts significantly lower values of both *SHF* and *LHF* compared to the MYJ scheme during the daytime, with average ΔSHF and ΔLHF reaching up to -18 W m^{-2} and -12 W m^{-2} respectively at noon. This relatively weaker transport of turbulent heat fluxes from the surface to the atmosphere during the daytime results in colder and drier air near the surface than that from the MYJ scheme. Over the sea, the YSU scheme produces slightly smaller *SHF* (ΔSHF: $-3 \sim -1$ W m^{-2}) and significantly larger *LHF* (ΔLHF: $20 \sim 30$ W m^{-2}) compared to the MYJ scheme through the entire day, indicating that more moisture is transported from the sea surface into the atmosphere in the YSU scheme. However, this stronger moisture transport in the YSU scheme did not result in a more humid near-surface air over the sea but rather relatively drier air compared to MYJ, with $-1.0 < \Delta q_2 < -0.7$ g kg^{-1}. This inconsistency between surface moisture flux and near-surface humidity may be attributed to diagnostic errors in the WRF thermodynamic

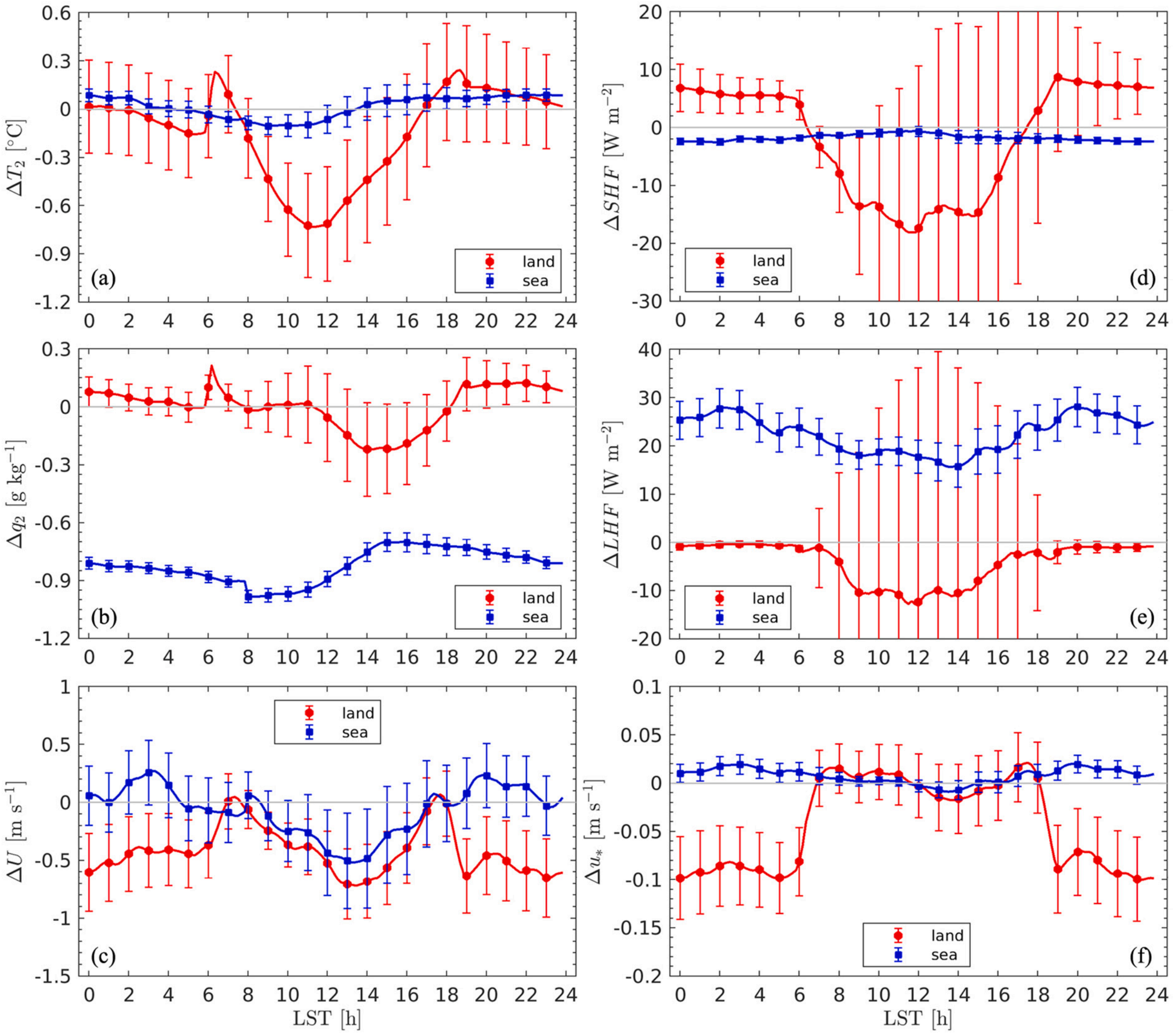

Fig. 7. Mean diurnal variations of the differences between the two PBL schemes (Δ = YSU − MYJ) for near-surface meteorological variables over the land and sea in July 2020. (a–c) 2-m temperature (*T*), 2-m specific humidity (*q*), and 10-m wind speed (*U*); (d–f) surface sensible heat flux (*SHF*), latent heat flux (*LHF*), and friction velocity (u_*). For clarity, the error bar representing the standard deviation is only shown per hour.

variables at 2 m height or to the physical processes represented by the model. We note that the YSU scheme simulates lower daytime 10-m U than the MYJ scheme both over the sea and over land, while it yields a slightly higher U than the MYJ scheme over the sea and lower U over the land at night. Regarding u_*, the daytime Δu_* is almost the same over the sea and land and close to zero, while the nighttime Δu_* close to 0.1 m s^{-1} over the sea and approximately 0.01 m s^{-1} over the land. This indicates that the two schemes have similar representations of momentum flux under unstable conditions both over the land and sea, but they have large differences under stable conditions over the land due to the sensitivity of the stability function to the surface roughness.

3.3.2. PBL height and vertical structure over the land and sea

To further investigate the performance differences between local and nonlocal PBL schemes in the temporal evolution of terrestrial and marine PBL structures, the mean daily variation and PDF of PBLH simulated by the two schemes are illustrated in Fig. 8. It is observed that the PBLH diagnosed by both schemes does not exhibit a significant diurnal variation over the sea, while over the land it rapidly increases after sunrise, peaks around 13:00 LST, and remains constant during the nighttime. As expected, the YSU scheme, which considers the entrainment mixing at the PBL top, produces deeper PBL than the MYJ scheme (Fig. 8a,c). Specifically, the PBLH difference between the YSU and MYJ schemes (Δh) consistently maintains at 100 $\sim$ 150 m throughout the entire day over the sea, and this systematic difference is confirmed by the almost identical PDF distribution of daytime and nighttime in Fig. 7d. Over the land, Δh remains the same at night but increases rapidly after sunrise during the daytime, reaching up to 400 m at 13:00 LST.

These performance differences between the YSU and MYJ schemes are primarily due to the local mixing term, which is responsible for the evolution of the all-day oceanic and nocturnal terrestrial PBLH. Conversely, the daytime entrainment mixing at the PBL top, together with the local mixing, plays a crucial role over the land (see Fig. 9). As shown in Fig. 9, the differences in K_h-profile between the YSU and MYJ schemes are relatively small over the sea, as well as over the land at night. These small differences of K_h result in the two PBL schemes having equivalent local mixing terms ($K_h\frac{\partial\theta}{\partial z}$), with maximum values ranging from 0.01 to 0.02 K m s^{-1}. Due to the small surface *SHF* (the average is about -4 W m^{-2} for nighttime land and < 5 W m^{-2} for daytime and nighttime sea), the entrainment mixing term ($-\left(\overline{w'\theta'}\right)_h\left(\frac{z}{h}\right)^3$) in the YSU scheme can be considered negligible for these situations, with maximum values at the PBL top ranging from 0.01×10^{-2} to 0.025×10^{-2} K m s^{-1}, which are only approximately 1% of the corresponding local mixing terms. In contrast, over land during the daytime, the YSU scheme shows a maximum K_h-profile value of about 145 m^2 s^{-1}, almost twice the value of MYJ. This larger K_h leads to the maximum value of $K_h\frac{\partial\theta}{\partial z}$ (0.22 K m s^{-1}) being approximately 1.83 times that of the MYJ scheme (0.12 K m s^{-1}). Moreover, due to the large land surface buoyancy flux during the daytime (with mean $SHF = 182 \pm 136$ W m^{-2}), the YSU scheme's entrainment mixing term can reach 3.3×10^{-2} K m s^{-1} at the PBL top, which is roughly 15% and 27% of the maximum local mixing term for the YSU and MYJ schemes, respectively. This suggests that entrainment mixing plays an important role in the evolution of the thermal-driven CBL.

It is noteworthy that there is a distinctive peak or trough in the differences of near-surface variables and PBLH between the YSU and MYJ schemes within 1 $\sim$ 2 h of sunrise and/or sunset over the land, as demonstrated by ΔT_2, Δq_2, ΔU, and Δu_* in Fig. 7, and Δh in Fig. 8. This

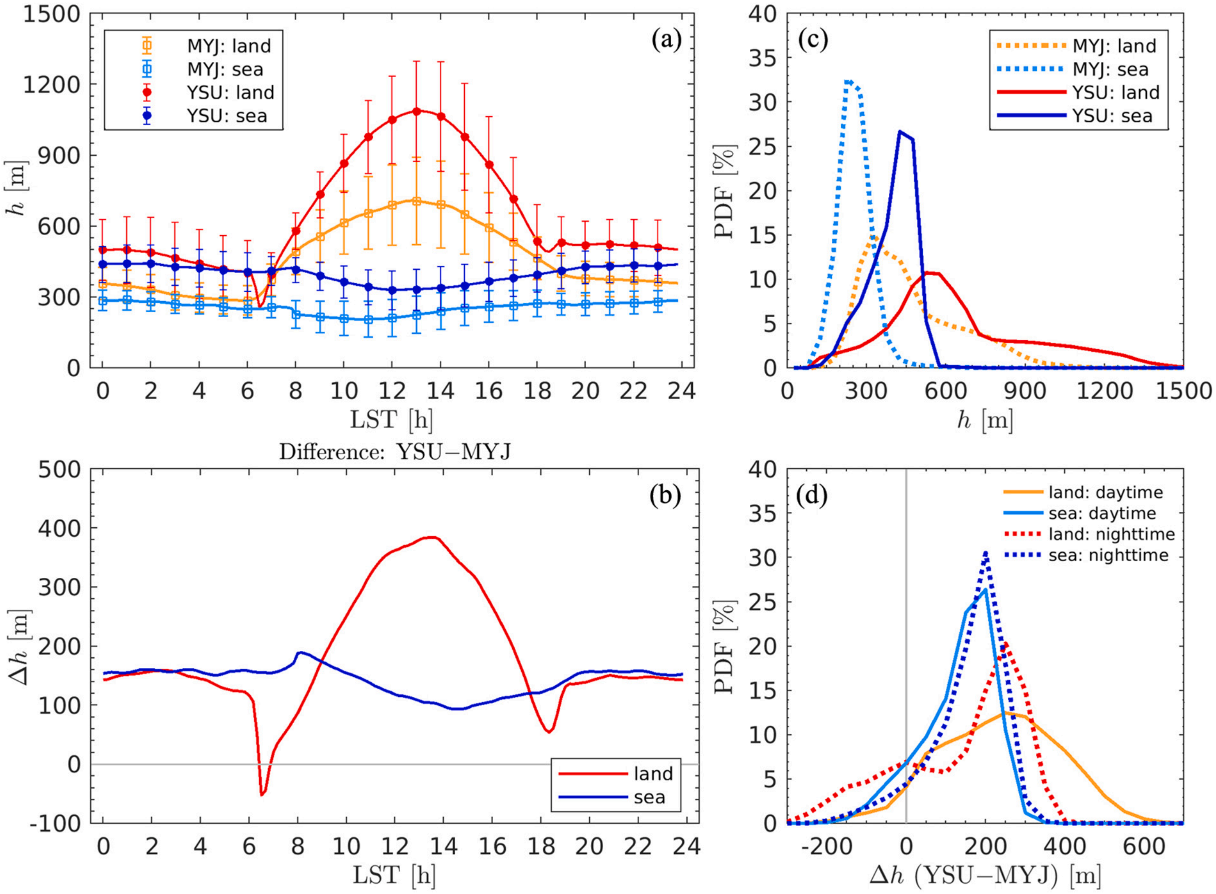

Fig. 8. (a, c) Mean diurnal cycle of PBLH (h) and PBLH difference between YSU and MYJ schemes (Δh) over the land and sea during one-month MESO1 simulations. (b, d) Probability density function (PDF) of h and Δh over the land and sea.

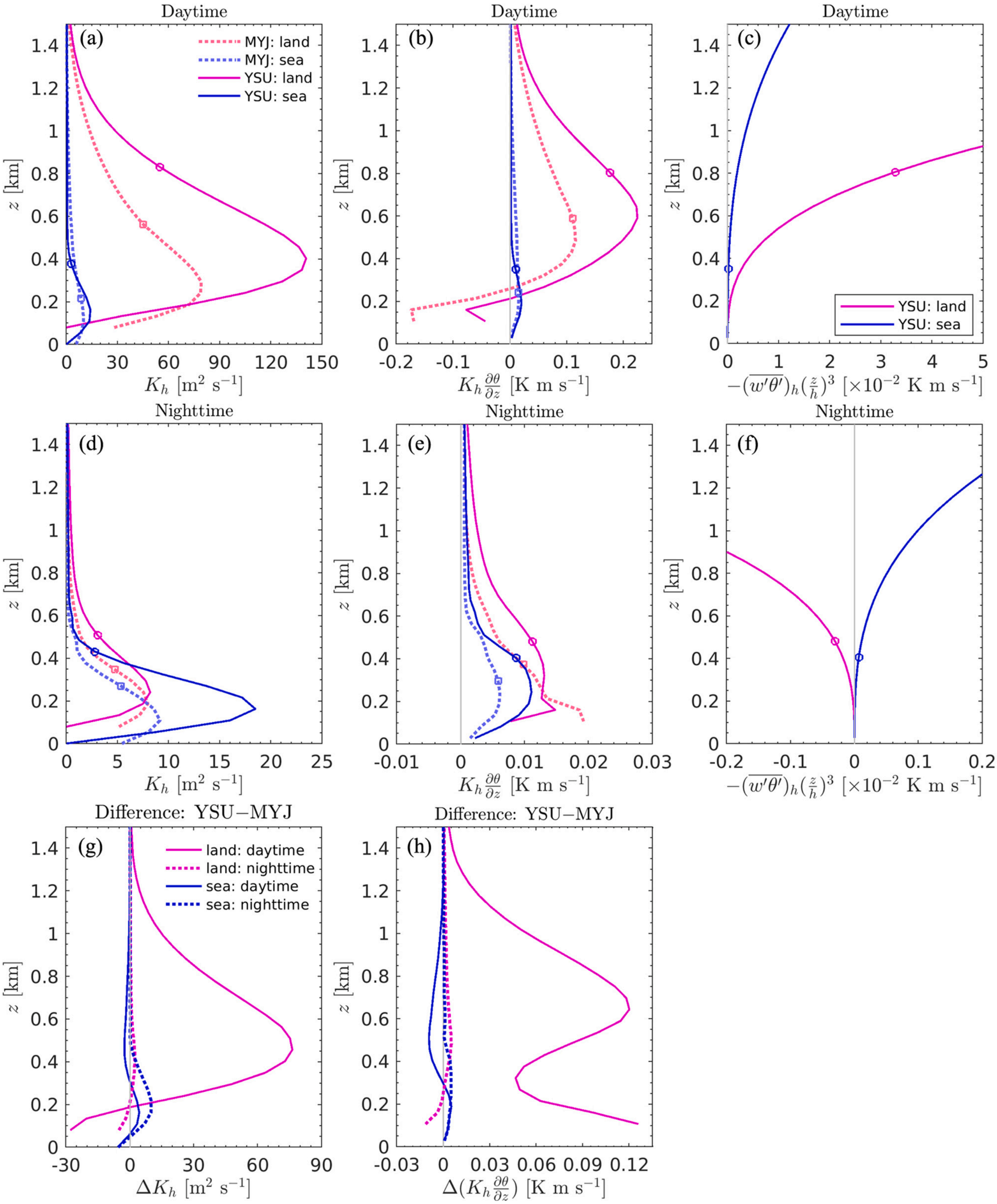

Fig. 9. Monthly mean vertical profiles of (a, d, g) turbulence thermal diffusivity K_h (m^2 s^{-1}), (b, e, h) local mixing term $K_h\frac{\partial\theta}{\partial z}$ (i.e., the 1st term on the right hand of Eq. (1) and Eq. (3); K m s^{-1}), and (c, f) entrainment mixing term $-(\overline{w'\theta'})_h\left(\frac{z}{h}\right)^3$ (i.e., the 3rd term on the right hand of Eq. (3); K m s^{-1}) over the land and sea during (a–c) daytime and (d–f) nighttime, as well as (g–h) their differences between YSU and MYJ schemes (Δ = YSU − MYJ). All profiles are spatial and temporal averages on all land/sea grid points in July 2020 from MESO1 simulations with 10 min time intervals. The colored symbols mark the location of the mean PBLH diagnosed by the corresponding PBL scheme. Note that the values of entrainment mixing shown above the PBLH in (c, f) are spurious, and should be disregarded.

sudden change in daily trends implies that both local and nonlocal PBL schemes have greater uncertainty at the morning and early evening transitions. During these periods, the PBL atmosphere transits from the nighttime stable boundary layer to daytime CBL after sunrise and reversely after sunset. This phenomenon is likely to be attributed to the dominance of vertical surface flux convergence during the transition periods, which limits the turbulent mixed layer to the shallow stable layer near the surface. The turbulent eddies tend to be small in size, exacerbating the influence of the surface heterogeneity, especially in areas with complex topography and land use, and thus resulting in the spatial variability of the near-surface thermodynamic variables peaking during the transition periods (Acevedo and Fitzjarrald, 2001; Bonin et al., 2013). Additionally, because the transitional periods are often ignored or not specifically parameterized in models (Mahrt, 1981), it leads to a higher level of simulation uncertainty during these periods.

Fig. 10 shows the averaged profiles of θ, q, U, and vertical velocity (w) simulated by different PBL schemes over the land and sea during the daytime and nighttime. To characterize the vertical motions over the land and sea more clearly, the vertical velocity is averaged only over four hours, i.e., 12:00 to 16:00 LST for daytime and 00:00 to 04:00 LST for nighttime. As expected, during the daytime, the simulated PBL air over the land is considerably warmer and drier ($\sim$ 2 K warmer and $\sim$ 1 g kg^{-1} drier near the surface, see Fig. A3) than that over the sea, with an upward motion ($w > 0$ m s^{-1}) over the land and downward motion ($w < 0$ m s^{-1}) over the sea (Fig. 10d). During the nighttime, the temperature and humidity differences between the land and sea become smaller (about -0.2 K and -0.3 g kg^{-1} near the surface, see Fig. A3), with an upward motion over the sea and downward motion over the land (Fig. 10h). This typical variation in temperature between land and sea would form the daytime sea breeze and nighttime land breeze, collectively known as the land-sea circulation. Both the YSU and MYJ

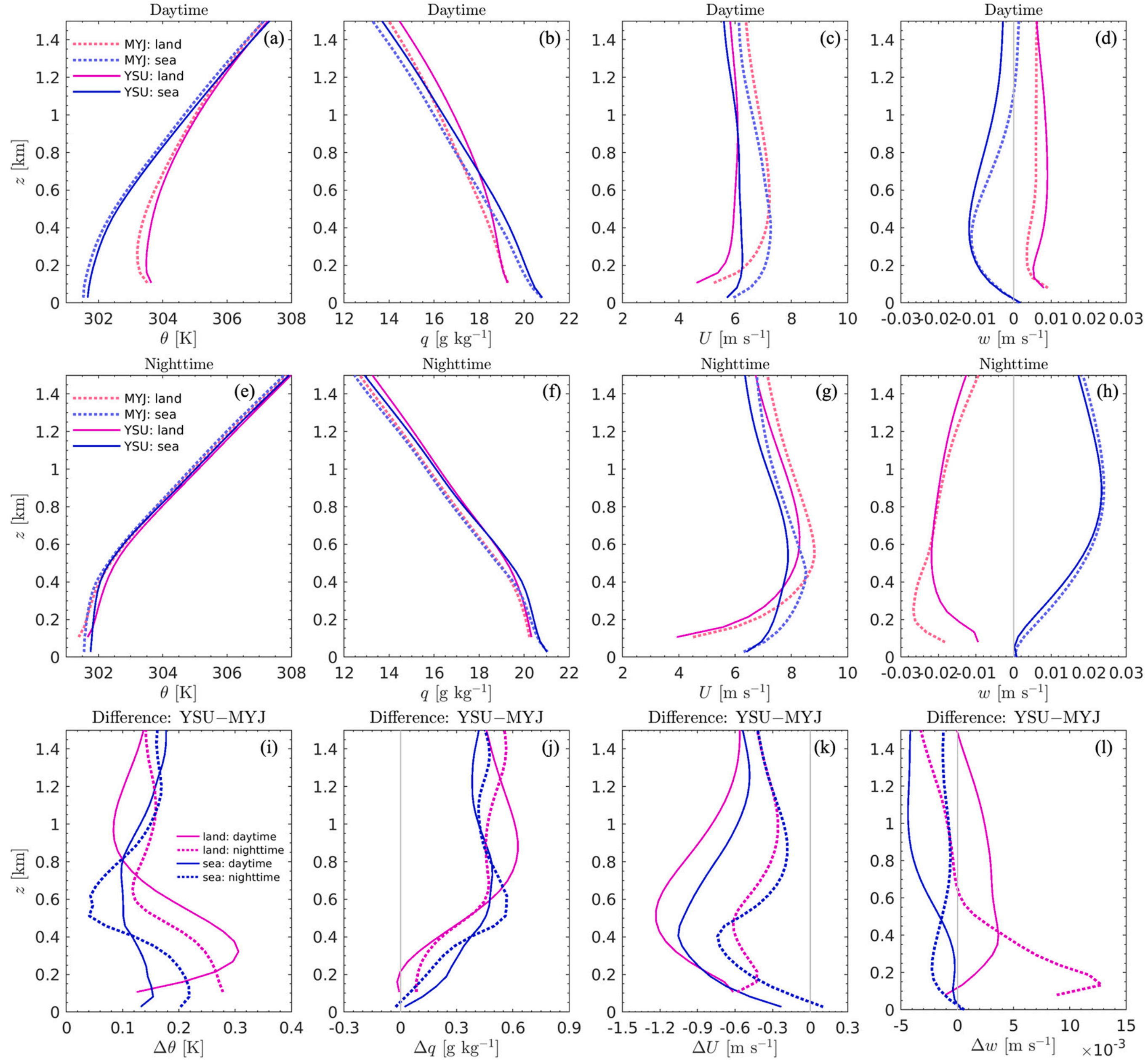

Fig. 10. Mean vertical profiles of (a, e, i) potential temperature (θ), (b, f, j) specific humidity (q), (c, g, k) horizontal wind speed (U), and (d, h, l) vertical wind speed (w) over land and sea during (a–d) daytime and (e–h) nighttime, as well as (i–l) the differences between YSU and MYJ schemes (Δ = YSU − MYJ). All profiles are spatial and temporal averages on all land/sea grid points during July 2020 from MESO1 simulations with 10 min time intervals.

schemes reproduce this typical difference in land and sea thermodynamics.

Compared to the MYJ scheme, the YSU scheme generally produces a warmer and moister lower troposphere with weaker wind speed, as indicated by the positive $\Delta\theta$ and Δq, and negative ΔU shown in Fig. 10i–k. This is due to the stronger turbulent mixing effect in the YSU scheme, which enhances the exchange of heat and water vapor between the underlying surface and the atmosphere, resulting in a more efficient heat and moisture transfer. It should be noted that the differences between the YSU and MYJ schemes vary for different variables and also with height over the land and sea. In addition, we find that the performance of the YSU scheme for thermodynamic variables at 2 m (relatively colder and drier; see Fig. 7a,b) is inconsistent with those above it (warmer and moister; see Fig. 10i,j) compared to the MYJ scheme during the daytime. This discrepancy is probably caused by the coupling errors between the physical processes in the land surface and PBL and the diagnostic errors in 2-m variables.

Overall, these differences in the simulated thermodynamic and dynamic variables between the YSU and MYJ schemes suggest that, in addition to their different parameterizations of the turbulence closure and entrainment processes, surface land cover types also contribute significantly to these deviations. This highlights the importance of carefully selecting the PBL scheme for simulating the temporal evolution of the PBL over the different land cover types, particularly in regions with complex topography and land use, where the PBL evolution is highly sensitive to surface heterogeneity and transition periods.

3.4. Turbulent flux relationships

Analyzing physical relationships between atmospheric variables can provide insight into the PBL surface system. In this section, we evaluate the performance of the WRF model based on some physical relationships inherent in the atmosphere, such as the functional behaviors between surface friction velocity and near-surface wind, and between turbulent fluxes and atmospheric instability (z/L). Here, $L = -\overline{\theta}_v u_*^3 / \left[kg\overline{w'\theta_v'}\right]$ is Monin-Obukhov length, where θ_v is virtual potential temperature, $k = 0.4$ is von Kármán constant, $g = 9.8$ m s^{-2} is the acceleration of gravity, and $\overline{w'\theta_v'}$ is surface buoyancy flux. In our analysis, we set z to the eddy-covariance measurement height of 10 m. To perform this evaluation, we utilize data collected from EC measurements and MESO1 simulations at site S5 during a 1-month period in July 2020 with 10-min time intervals.

3.4.1. Friction velocity and wind speed

Fig. 11a reveals a strong linear correlation between u_* and U with $R > 0.95$ for both the observations and WRF simulations, with $u_* = 0.069U$ for observations, $u_* = 0.096U$ for MYJ simulation, and $u_* = 0.097U$ for YSU run. According to the bulk flux framework, the wind stress $\tau = \rho u_*^2 = \rho C_D U^2$ (where ρ is air density and C_D is drag coefficient), thus the slope of u_*-U relationship obtained by least squares fitting can be used to represent C_D. The drag coefficient is generally defined in the model as $C_D = k^2 / \left[\ln(z/z_0) - \Psi_m(z/L)\right]^2$, where z_0 is the surface roughness length and $\Psi_m(z/L)$ is the momentum stability function. Therefore, a larger roughness length or magnitude of stability function produces a larger C_D and hence a larger momentum transport. The C_D

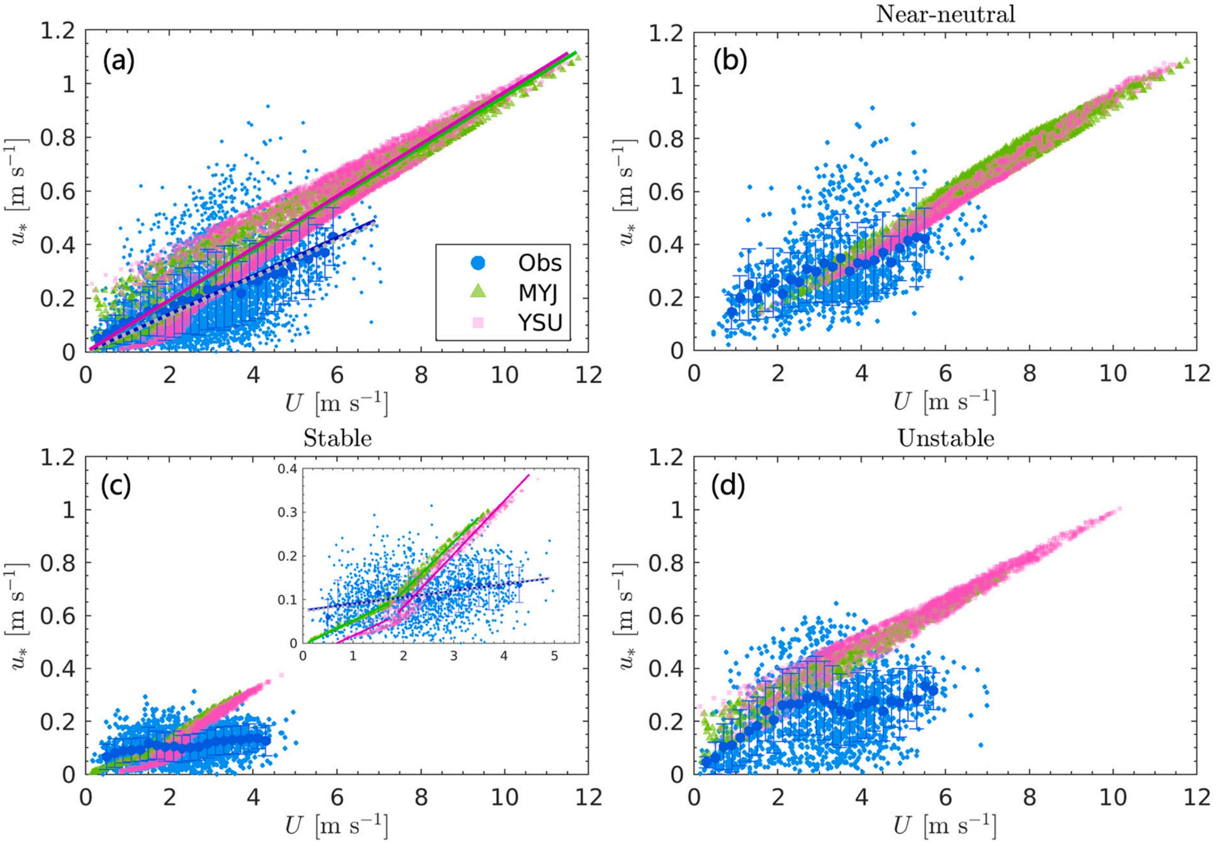

Fig. 11. Variation of surface friction velocity (u_*) with near-surface wind speed (U) in the observations (blue) and WRF simulations (green: MYJ, magenta: YSU) at site S5 during the 1-month simulation period with 10-min time intervals. (a) All data for a month, (b) under near-neutral conditions ($-0.1 \le z/L \le 0.1$), (c) under stable conditions ($z/L > 0.1$), with a small panel as zoom, and (d) under unstable conditions ($z/L < -0.1$). The large blue dots with error bars are bin averages and standard deviations of the observation. The colored lines are least-squares fittings: green for MYJ, magenta for YSU, blue for bins averaged observations, and gray dashed line for original observations. (For interpretation of the references to colour in this figure legend, the reader is referred to the web version of this article.)

values obtained from the u_*-U slope for the observations, MYJ, and YSU are approximately 4.76×10^{-3}, 9.22×10^{-3}, and 9.41×10^{-3}, respectively. This shows that the WRF model with both PBL schemes overestimates C_D, with the values being almost twice the observed C_D. This strong momentum transfer in the model is most likely caused by its large z_0. The underlying surface in a large area surrounding site S5 and its upwind direction (to the south) consisted of croplands and wetlands, with their z_0 varying in the range of $0.14 \sim 0.3$ m in the model, which is larger than the observed z_0 of ~ 0.1 m estimated by He et al. (2021) under southwest wind direction.

The u_*-U relationship is also analyzed under different atmospheric stratification conditions, as shown in Fig. 11b–d. Under near-neutral conditions ($-0.1 \le z/L \le 0.1$), both simulations and observations show a linear relationship with a similar u_*-U slope of ~ 0.09 (hence similar $C_D \sim 8 \times 10^{-3}$), indicating that the two PBL schemes reproduce the momentum transport processes well under near-neutral conditions. For stable conditions ($z/L > 0.1$), the observed data show a linear relationship with a slope of 0.04, while both the MYJ and YSU schemes display two distinct regimes, resembling a hockey stick transition demonstrated by Sun et al. (2020). When $U \le 1.8$ m s^{-1}, their slopes are about 0.055, which is about 1.6 times the observed value of 0.035 at low wind speed. When $U > 1.8$ m s^{-1}, the simulation-derived slope suddenly increases to 0.113 for MYJ and 0.121 for YSU, which is slightly larger than that under near-neutral conditions and significantly greater than the corresponding observed value (~ 0.025). In addition to the larger z_0 in the model discussed earlier, this overestimation of the u_*/U ratios (and therefore C_D) and the existence of two regimes are likely related to the stability function used in the surface-layer model linked to both PBL schemes. Under unstable conditions ($z/L < -0.1$), both the YSU and MYJ schemes yield a similar u_*/U ratio of 0.110 (therefore the average $C_D = 12.1 \times 10^{-3}$), which is the same as the second regime of stable conditions. However, the observation-derived u_*/U ratio exhibits two distinct regimes: 0.10 for weak wind ($U < 3.0$ m s^{-1}) and 0.023 for moderate wind ($3 \le U \le 6$ m s^{-1}).

3.4.2. *Drag coefficient and instability*

To further investigate the variation of drag coefficient with the atmospheric instability, we examine the relationships between C_D (derived from the u_*/U ratio) and z/L in both observations and simulations, as shown in Fig. 12. Since the observed data points are largely scattered, we perform a bin-average calculation to obtain a more representative value of observed C_D. The results show that C_D almost remains constant for both observed and simulated data under near-neutral conditions ($-0.1 \le z/L \le 0.1$), with C_{DN} (neutral C_D) values of $(12.69 \pm 15.37) \times 10^{-3}$, $(8.59 \pm 0.93) \times 10^{-3}$, and $(7.96 \pm 0.91) \times 10^{-3}$ for observations, MYJ, and YSU, respectively. The relatively smaller C_{DN} in the model is likely responsible for the overestimation of near-surface wind speed and friction velocity. Under stable conditions ($z/L > 0.1$), both observed and simulated C_D gradually decrease as z/L increases. However, the MYJ scheme shows a constant value of $\sim 2.4 \times 10^{-3}$ when $z/L > 1$, while the YSU scheme reproduces the observed C_D-z/L behavior well, although its values are slightly lower than the observations. This difference in performance may be due to the adoption of Ri_b in the YSU scheme instead of z/L and its stability function, which has two regimes under stable conditions: $0 < Ri_b \le 0.2$ and $Ri_b > 0.2$. Under unstable conditions ($z/L < -0.1$), both observed and simulated C_D slightly increase with increased instability when $-0.5 < z/L < -0.1$ (weak unstable). However, when the atmospheric stratification becomes strongly unstable ($z/L < -1.0$), the observed C_D declines significantly, while the simulated C_D shows an exponential increase with $-z/L$. The latter may contribute to an underestimation of the small proportion of wind speeds in Fig. 3b,f and Fig. A4b,c. Furthermore, the observations reveal that strong instability inhibits momentum transfer, a feature that neither of the PBL schemes can reproduce.

After conducting the least-squares fitting (LSF) test, we find that the relationship between C_D and z/L in both observations and simulations can basically be represented by the function $C_D = \alpha\left(1 + \beta\frac{z}{L}\right)^{-1}$ under both stable and unstable conditions. The fitting coefficient α is slightly larger for $z/L < 0$ than that for $z/L > 0$ for both observations and simulations. To maintain consistency, we force the coefficient α for unstable conditions to be equal to the value under stable conditions. The fitted α values are 12.77×10^{-3}, 8.41×10^{-3}, and 8.53×10^{-3} for observations, MYJ, and YSU, respectively, which closely match the corresponding averaged C_{DN} obtained earlier. Therefore, the fitted α can be seen as C_{DN}. The β values of observations, MYJ, and YSU are 2.81, 2.44, and 3.22 for $z/L > 0$ and -0.24, 0.87, and 0.61 for $z/L < 0$, respectively. All fitted curves are highly significant ($p < 0.001$) with a correlation coefficient >0.96 in observations and 0.99 in simulations. However, it should be noted that the fitting formula $C_D = C_{DN}\left(1 + \beta\frac{z}{L}\right)^{-1}$ is not applicable for the MYJ scheme when $|z/L| > 1$ or the YSU scheme when $z/L < -1$. These findings suggest that the stability function for momentum in the surface-layer model associated with the MYJ and YSU PBL schemes should be improved for strongly unstable conditions. Additionally, the stability function in the surface-layer model linked to the MYJ scheme also needs improvement for extremely stable conditions ($z/L > 1$).

3.4.3. *Turbulent fluxes and instability*

The near-surface turbulent fluxes (e.g., momentum flux, sensible heat flux, and latent heat flux) are essential parameters in the exchange of momentum, heat, and moisture between the surface and atmosphere, impacting the surface drag and energy balance. These turbulent fluxes are strongly influenced by atmospheric instability, which is a key

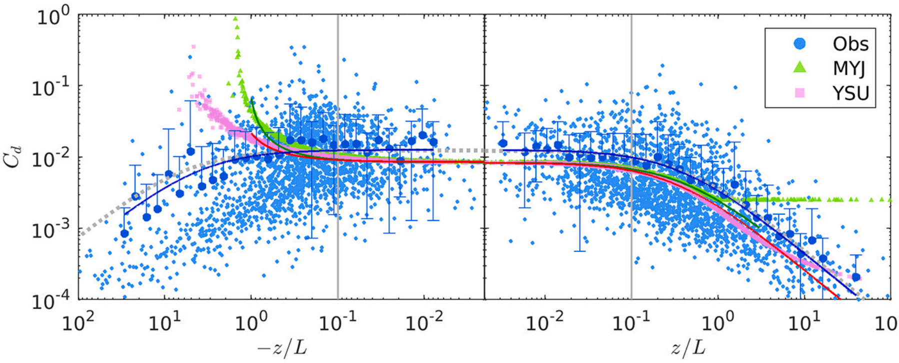

Fig. 12. Variation of drag coefficient (C_D) with atmospheric instability (z/L). The left and right panels represent unstable ($z/L < 0$) and stable ($z/L > 0$), respectively. The gray vertical lines are -0.1 and 0.1 lines of z/L. The large blue dots with error bars are bin averages and corresponding standard deviations for the observations. The colored curves are least-squares fitted lines: green for MYJ, red for YSU, blue for bins averaged observations, and gray dashed line for original observations. (For interpretation of the references to colour in this figure legend, the reader is referred to the web version of this article.)

parameter characterizing the dynamics of the PBL. Therefore, comprehending the relationships between turbulent fluxes and atmospheric instability is crucial for improving our understanding of the PBL dynamics and for developing more accurate NWP and climate models.

Fig. 13 illustrates the variation of u_* (representing vertical momentum flux), *SHF*, and *LHF* with respect to z/L. Although the simulated turbulent fluxes are significantly greater than the observed ones under unstable conditions, both the MYJ and YSU schemes reproduce the evolution of turbulent fluxes with atmospheric instability in a manner consistent with observations. Specifically, u_* rapidly increases

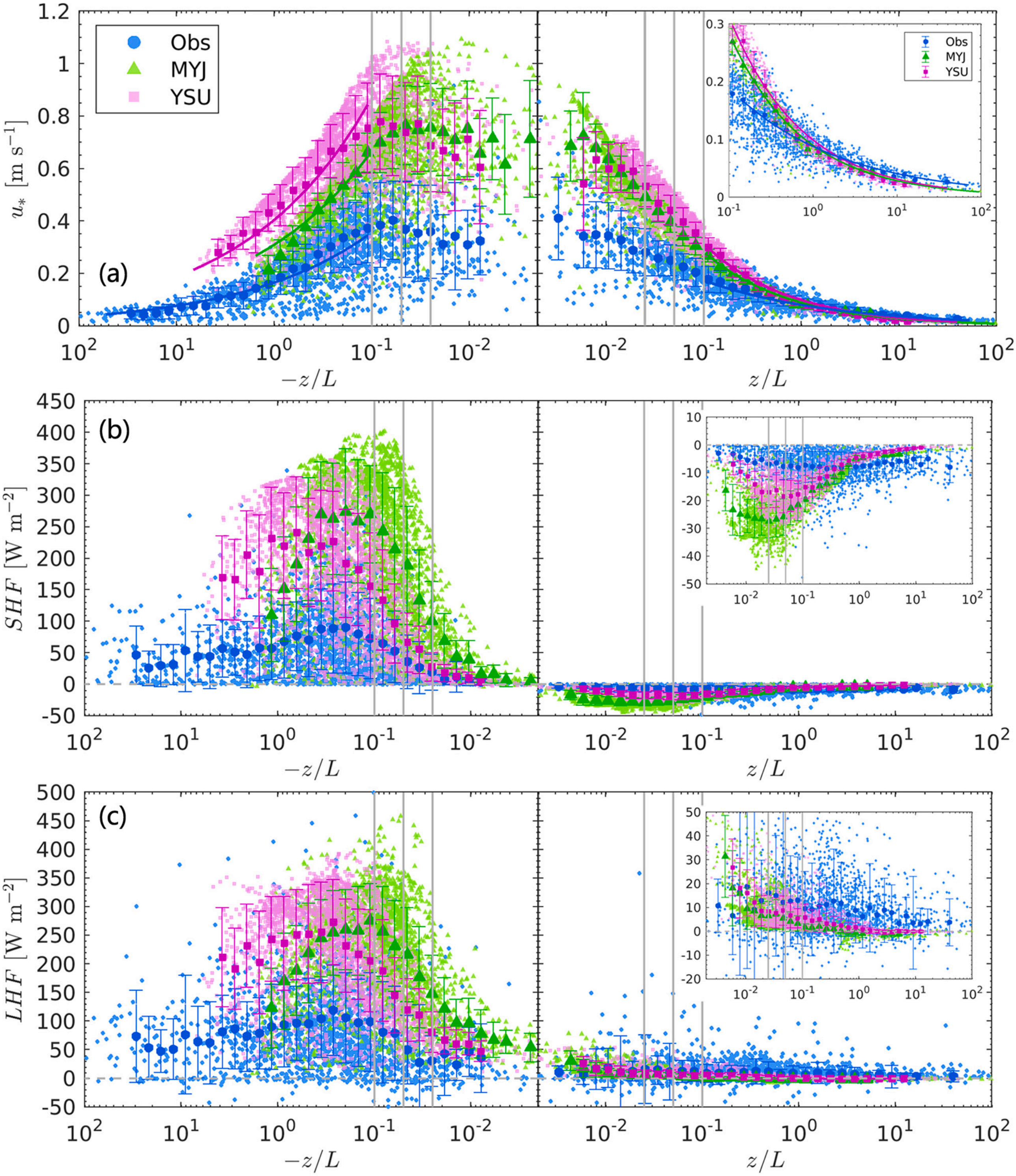

Fig. 13. Variation of surface turbulent fluxes with atmospheric instability (z/L): (a) momentum flux (u_*), (b) sensible heat flux (*SHF*), and (c) latent heat flux (*LHF*). The left and right panels represent unstable ($z/L < 0$) and stable ($z/L > 0$) conditions, respectively. Large markers with error bars are bin averages and their corresponding standard deviations. The vertical gray lines are ± 0.025, ± 0.05, and ± 0.1 lines of z/L, and the horizontal gray dashed line is the zero line. The small panel is a zoom of the corresponding variable in stable conditions. The curves in (a) are the least-squares fitted lines (green: MYJ; magenta: YSU; blue: bins-averaged observations). (For interpretation of the references to colour in this figure legend, the reader is referred to the web version of this article.)

from the strongly unstable/stable to near-neutral conditions, forming a right-skewed bell-shaped distribution with a peak occurring in the range of $-0.1 < z/L < -0.01$ on the unstable side. One notable feature of both *SHF* and *LHF* is their rapid increase from nearly 0 W m^{-2} at neutral condition ($z/L \approx 0$) with the increase of the instability, reaching a peak in the moderate and weakly unstable range of $-1.0 < z/L < -0.05$ with bin-averages of approximately 100 W m^{-2} for observations and 250 $\sim$ 300 W m^{-2} for simulations. Under unstable conditions, this distribution of *SHF* and *LHF* exhibits a right-skewed bell shape. This bell-shaped distribution feature of u_*, *SHF*, and *LHF* was also found by Yusup and Liu (2016) over the water surface of a reservoir in Mississippi. Furthermore, a clear transport dissimilarity between momentum and heat fluxes exists under both stable and unstable conditions. On the unstable side, as instability increases from neutral towards near-neutral, a slight increase in u_* corresponds to a rapid rise in both *SHF* and *LHF*. As instability transitions from moderately unstable at $z/L \approx -0.2$ to strongly unstable ($z/L < -1$), a rapid attenuation of u_* is accompanied by a gradual decrease in both *SHF* and *LHF*. However, on the stable side, as stability moves from neutral to strongly stable, a declining u_* corresponds to a continued and slow decline of *LHF*, while the negative *SHF* first increases with stability with peaks around $z/L = 0.1$, and then decreases with further stability. These inconsistent findings indicate that an increase in mechanical mixing alone does not necessarily result in increased turbulent heat fluxes (Yusup and Liu, 2016). Thermal mixing is another important factor that affects the transfer of turbulent heat fluxes, particularly during the daytime over the land.

The relationship between both observed and simulated u_* and z/L can be described by the equation $u_* = \alpha\left|\frac{z}{L}\right|^{-1/3}$ for both stable and unstable conditions where $|z/L| > 0.1$, indicating decay of momentum transfer with increasing instability or stability. The fitted coefficients α for observations, MYJ, and YSU are approximately 0.181 (0.088), 0.310 (0.110), and 0.405 (0.126) under unstable (stable) conditions. These fittings exhibit strong correlation coefficients with corresponding values of 0.989 (0.998), 0.834 (0.924), and 0.715 (0.917), all of which are highly significant ($p < 0.001$). However, the simulated relationship between u_* and z/L under stable conditions is more consistent with a power of $-1/2$ instead of $-1/3$, i.e., $u_* = \alpha\left(\frac{z}{L}\right)^{-1/2}$, where α of the MYJ and YSU schemes are 0.090 and 0.099, with corresponding correlation coefficients of 0.975 and 0.971 ($p < 0.001$). The coefficient α derived from simulations is significantly larger than that from the observations, indicating that the momentum transfer in the model decreases too fast with instability/stability. Consequently, the simulated near-surface wind speed decreases with instability/stability faster than the observations, with a significant overestimation when $-0.1 < z/L < 0.02$ and underestimation under strongly unstable and stable conditions (refer to Fig. A4b,c). We find that the most accurately simulated U occurs at $0.05 < z/L < 2$ (especially for the YSU scheme; see Fig. A4b,c), which corresponds to the good u_*-z/L relationship in Fig. 13a, indicating that the WRF model reproduces the mechanical mixing process well in this regime.

Since the surface turbulent fluxes in NWP and climate models are usually described by the Monin-Obukhov similarity theory (Stull, 1988) with the bulk transfer coefficients determined by the atmospheric instability, it is widely believed that turbulent heat fluxes exchanges are depressed under stable conditions and promoted under unstable conditions (Yusup and Liu, 2016). We find that the averaged *SHF/LHF* in unstable ranges $z/L < 0$ (60 $\sim$ 80 W m^{-2} for observations and 175 $\sim$ 215 W m^{-2} for simulations) are significantly larger than those in stable ranges $z/L > 0$ (about -10 and 10 W m^{-2} respectively for observations and simulations). This larger averaged *SHF* and *LHF* under unstable conditions are partly attributed to the larger values of u_* (~ 0.3 m s^{-1} for observations and ~ 0.6 m s^{-1} for simulations) and U (~ 3 m s^{-1} for observations and ~ 6 m s^{-1} for simulations) compared to stable conditions (u_* and U are 54 $\sim$ 66 % and 72 $\sim$ 78 % of the corresponding values under unstable conditions, respectively). Compared to the MYJ scheme, the YSU scheme generates relatively small u_* under both stable and unstable conditions, resulting in its simulated U being closer to the observed values and leading to relatively more accurate *SHF* and *LHF*. Under unstable conditions, it is generally expected that *SHF* and *LHF* will increase with increased instability. This is because the intensified turbulence and mixing promote the growth of convective eddies, which enhance the transport of heat and moisture from the surface to the atmosphere. However, we find that *SHF* and *LHF* do not always rise with increased instability under unstable conditions. Instead, they tend to decline gradually with strengthened instability (towards very unstable conditions) when $z/L < -0.5$. This behavior indicates that strong instability can inhibit the exchange of turbulent fluxes. This occurs when instability becomes strong to a certain extent that large-scale energetic turbulent eddies overwhelm the smaller-scale turbulent motions responsible for heat and moisture exchange between the surface and the atmosphere. Additionally, strong instability can enhance turbulent mixing, resulting in a well-mixed layer that, in conjunction with entrainment mixing, reduces the temperature and moisture gradients between the surface and the atmosphere. This, in turn, decreases the driving force for further heat transfer.

Given the absence of temperature and humidity gradients, we investigate the modulation of thermal mixing on turbulent heat fluxes at different levels of atmospheric instability using U-normalized *SHF* and *LHF*, as shown in Fig. 14. It is clear that the bell-shaped distributions of *SHF* and *LHF* observed under unstable conditions, as well as the inverted bell-shaped distribution of *SHF* under stable conditions in Fig. 13b,c disappear. This suggests that the mechanical-induced turbulent mixing is the primary cause of the bell-shaped distribution. Furthermore, the simulated SHF/U and LHF/U match observations well when $-0.5 < z/L < 0$ in the unstable side. Similarly, when $0 < z/L < 0.5$ in the stable side, the simulated SHF/U also agrees well with observations, particularly for the YSU scheme. These findings suggest that the model's significant overestimation of *SHF* and *LHF* at $-0.5 < z/L < 0$, and the overestimation of negative *SHF* at $0 < z/L < 0.5$, are mainly attributed to the simulated strong mechanical mixing, as quantified by u_* (see Fig. 13a), and the resulting higher wind speeds (as shown in Fig. A4b,c). However, for $z/L < -0.5$, both observed SHF/U and LHF/U slightly decrease with increasing instability, similar to the variations of *SHF* and *LHF*. In contrast, the simulated SHF/U and LHF/U increase exponentially with instability, rather than the slow decreasing trend of *SHF* and *LHF*. This implies that the overestimation of *SHF* and *LHF* at $z/L < -0.5$ is most likely caused by inaccurate thermal mixing in the model.

4. Conclusions and discussion

In this study, we investigate the impacts of PBL schemes on WRF simulations of atmospheric boundary layer processes over a tropical coastal region with complex terrain. Two commonly used PBL schemes (the local scheme MYJ and the nonlocal scheme YSU) were selected to perform multiscale simulations spanning one month (July) in the summer of 2020 over Shenhen, China, with horizontal resolutions of 27, 9, 3, and 1 km. The simulations were comprehensively evaluated against multisource observations, including automatic weather station observations, eddy-covariance measurements, and GPS-sounding profiles. In addition to the traditional assessments by direct comparison with observations, we also investigated the sensitivity of PBL schemes to horizontal resolutions and land cover types and evaluated the model performance through inherent physical relationships between near-surface variables.

The results demonstrate that the WRF model, with both local and nonlocal PBL schemes, can capture well the observed diurnal variations of all near-surface meteorological variables (including the turbulent fluxes) and the PBL vertical thermodynamic structures over the complex terrain. However, it tends to underestimate air temperature and overestimate wind speed throughout the entire PBL and almost during the

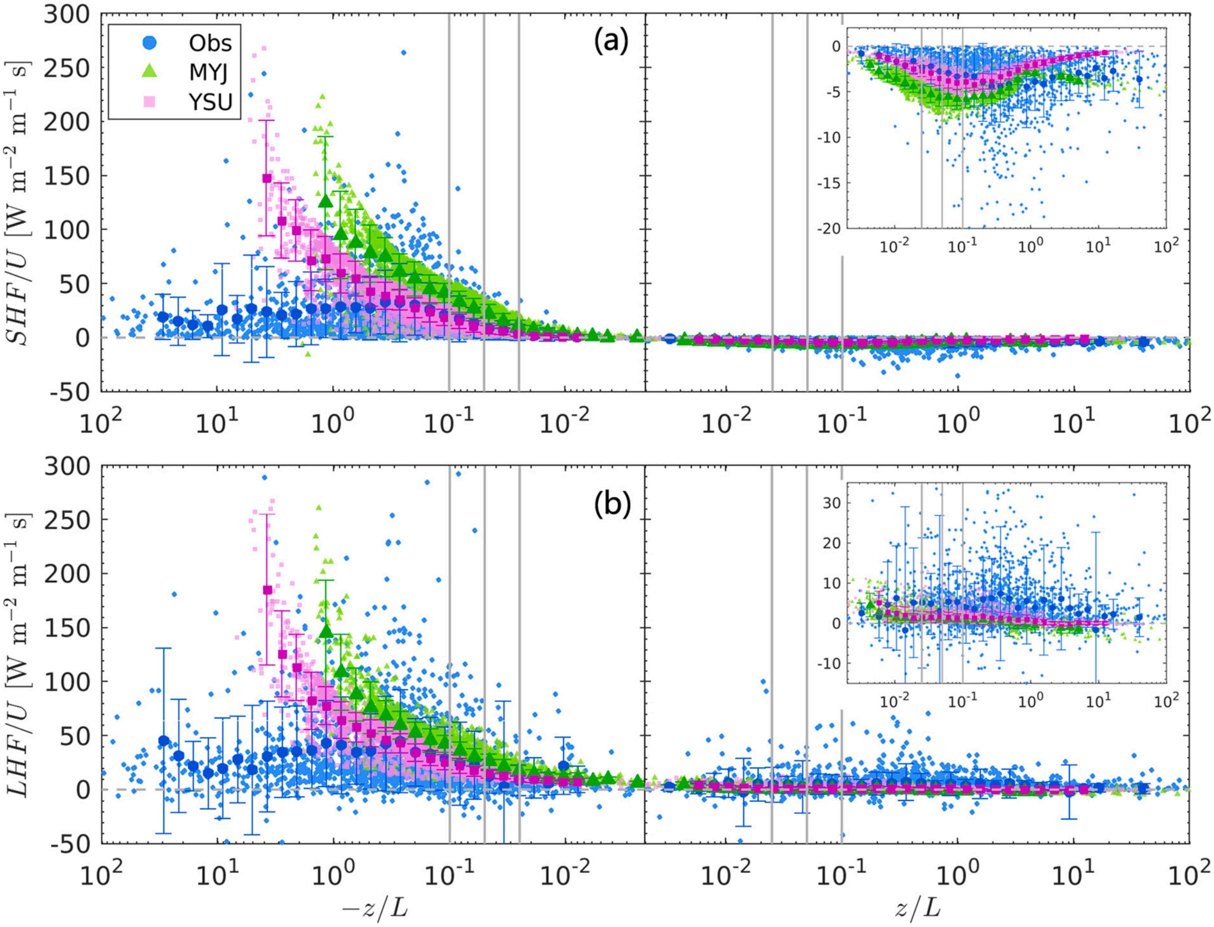

Fig. 14. Variation of normalized surface turbulent heat fluxes with atmospheric instability (z/L): (a) SHF/U (W m^{-2} m^{-1} s), (b) LHF/U (W m^{-2} m^{-1} s). The left and right panels represent unstable ($z/L < 0$) and stable ($z/L > 0$) conditions, respectively. Large markers with error bars are bin averages and their corresponding standard deviations. The vertical gray lines are ±0.025, ±0.05, and ±0.1 lines of z/L, and the horizontal gray dashed line is the zero line. The small panel is a zoom of the corresponding variable in stable conditions.

whole day, with mean biases ranging from $-0.5 \sim -0.2\,^{\circ}$C for 2-m T and $2 \sim 5$ m s^{-1} for 10-m U. The overestimation of wind speed rapidly decreases with altitudes. The findings suggest that the simulation errors likely stem from the land surface, such as inaccurate coarse-resolution land-use data and non-application of urban canopy models. Moreover, the WRF model significantly overestimates surface turbulent heat and momentum fluxes throughout the whole day (including the nighttime negative *SHF*), especially with their daytime peaks $2 \sim 3$ times larger than observations, which is primarily caused by the overestimation of wind speed and likely to be an inherent flaw of the surface layer models (Sun et al., 2017; Sathyanadh et al., 2017). Furthermore, the diagnosed PBLH in the WRF model is consistently lower than the observations, with monthly averages from the local and nonlocal schemes about 47% and 28% lower than the observed values, respectively. However, after recalculating the PBLH using the same method, the results for the local and nonlocal schemes are almost identical, ~17% lower than the observation. This result suggests that reducing (increasing) the threshold value of TKE (Ri_b) in the MYJ (YSU) scheme could improve the accuracy of PBLH diagnosis and reduce uncertainties from different methods.

We found that the performance of the WRF model over complex terrain with both local and nonlocal PBL schemes improves significantly with the increasing horizontal resolution, particularly for variables such as winds that depend highly on local topography features. Despite the best model performance for some variables (e.g., daytime sensible heat and momentum fluxes) being at the resolution of 3 km, the model at 1 km resolution provides the best results overall, with the most accurate daytime latent heat flux and all first-order variables as well as nighttime sensible heat flux. Therefore, for mesoscale simulations over complex terrain, we recommend using the high resolution of 1 km.

Similar to previous studies, the YSU scheme outperforms the MYJ scheme overall over the complex terrain, for both surface variables and PBL vertical structures, although the MYJ scheme performs slightly better in some cases. The YSU scheme produces more accurate potential temperature, humidity, and wind speed throughout the entire PBL for both morning and evening hours, and this conclusion is independent of the horizontal resolutions. Unlike previous studies, where the nonlocal PBL scheme tends to produce warmer and drier PBL, in our cases, the YSU runs generate warmer and moister PBL than the local scheme MYJ. This is due to the small gradient of humidity between the free atmosphere and PBL in the coastal region, where the entrainment mixing effect cannot significantly reduce the water vapor within the PBL, but is only conducive to warming the PBL and raising the PBL height. The monthly mean PBLH simulated by the YSU scheme is about 25% higher than that by the MYJ scheme, which is mainly caused by the stronger local mixing in the YSU scheme, with a maximum value of monthly mean K_h in the PBL almost 1.9 (2.8) times larger than that of MYJ runs at morning (evening) hours.

However, the differences between the two schemes are significantly distinct over different land covers, such as land and sea, and they vary with variables, time periods, and altitudes within the PBL. Generally, the differences between the two schemes are significantly greater over the land than over the sea for thermal-related variables (e.g., T, *SHF*, and

PBLH), especially during the daytime, while for variables associated with water vapor (e.g., q and LHF), they are significantly larger over the sea than over the land. These findings show that land surface feature has a crucial influence on the performance of PBL schemes, and highlight the importance of selecting appropriate PBL schemes for simulating the temporal evolution of PBL over different land cover types, particularly over the regions with complex terrain and land use. Furthermore, we found that the maximum value of local mixing term within PBL in the YSU scheme is about twice that of the MYJ scheme over land during the daytime, while it is comparable to the corresponding value in the MYJ scheme over the sea through the whole day and over land at night, with a relatively small value. The maximum of the entrainment mixing term in the YSU scheme is only <1% of the local mixing term over the sea and during nighttime over land due to their small surface sensible heat flux, while it can reach 15% of the peak value of the local mixing term over land during the daytime. These results suggest that the differences between nonlocal and local PBL schemes can largely be attributed to their different eddy diffusivity (local mixing), the entrainment mixing in the nonlocal scheme only plays a secondary role in the buoyancy-driven convective boundary layer, especially over land in the daytime.

The WRF model, with both local and nonlocal PBL schemes, generally captures the physical relationships between near-surface variables, such as the strong linear correlation between u_* and U, the power law between C_D or u_* and instability z/L, and the bell-shaped distribution of turbulent fluxes with z/L. Overall, the relationships obtained from the YSU simulations agree with the observations better than the MYJ runs. However, the model overestimates the u_*/U ratio, especially under stable conditions for $U > 1.8$ m s^{-1} and stable conditions for $U > 3$ m s^{-1}. The simulated C_{DN} is significantly smaller than the observed, resulting in a significant overestimation of wind speed under near-neutral conditions. Additionally, neither PBL scheme reproduces the decreasing trend of the observed C_D against z/L when $-z/L > 1$, causing the model to underestimate wind speed under strongly unstable conditions. Furthermore, the simulated bell-shaped curves for turbulent heat fluxes in unstable regions are significantly higher than the corresponding observations, with the peak in the range of $0.05 < -z/L < 1.0$, suggesting that the overestimation of turbulent heat fluxes occurs mainly under unstable conditions when $0.05 < -z/L < 1.0$. We found that the bell-shaped distribution disappears in the U-normalized turbulent heat fluxes, and the simulated SHF/U and LHF/U are consistent with observations well when $-z/L < 0.5$. However, they increase rapidly with z/L when $-z/L > 0.5$ (especially for $-z/L > 1$), and do not reproduce the observed slow decay trend. These findings suggest that the mechanical-induced turbulent mixing is the primary cause of the bell-shaped distribution of turbulent heat fluxes, and the overestimation of turbulent heat fluxes under unstable conditions is mainly attributed to stronger mechanical mixing in the model at $-z/L < 0.5$, and inaccurate thermal-induced turbulent mixing at $-z/L > 0.5$.

In summary, this study comprehensively evaluates the PBL schemes and the WRF model's performance over the tropical coastal region with complex terrain. The findings could help to improve the parameterizations of the PBL and associated surface layers. Further investigations are needed to consider the urban morphology effects and to focus on some key processes such as land-sea breeze circulation and terrain-induced flows. To raise the confidence level, the evaluation should be expanded to more observation sites, and to cover a wide range of atmospheric stability conditions.

CRediT authorship contribution statement

Yong-Feng Ma: Conceptualization, Methodology, Investigation, Validation, Visualization, Writing – original draft, Writing – review & editing, Funding acquisition. **Yuting Wang:** Conceptualization, Methodology, Investigation, Validation, Writing – original draft, Writing – review & editing. **Tao Xian:** Writing – review & editing. **Geng Tian:** Writing – review & editing. **Chao Lu:** Resources. **Xia Mao:** Resources. **Lian-Ping Wang:** Writing – review & editing, Funding acquisition.

Declaration of Competing Interest

The authors declare that they have no known competing financial interests or personal relationships that could have appeared to influence the work reported in this paper.

Data availability

The data used in this paper are downloaded from the following websites. SRTM: https://opentopography.org, last access on 15 Jun 2023; MODIS: https://lpdaac.usgs.gov/products/mcd12q1v006, last access on 15 Jun 2023; ERA5: https://rda.ucar.edu/datasets/ds630.0, last access on 15 Jun 2023; sounding profiles of Hong Kong: http://weather.uwyo.edu/upperair/sounding.html, last access on 15 Jun 2023. The simulation output will be made available on request.

Acknowledgments

This work was supported by the National Natural Science Foundation of China (42075078, 42075071), the Shenzhen Science and Technology Program (KQTD20180411143441009, JCYJ20220530113005012, 2020-148), and the Hong Kong Research Grants Council (T24-504/17-N). We would like to acknowledge the high-performance computing supported by the Center for Computational Science and Engineering at SUSTech and the National Key Scientific and Technological Infrastructure project “Earth System Numerical Simulation Facility” (EarthLab).

Appendix A. Additional figures for model validation are provided in this appendix

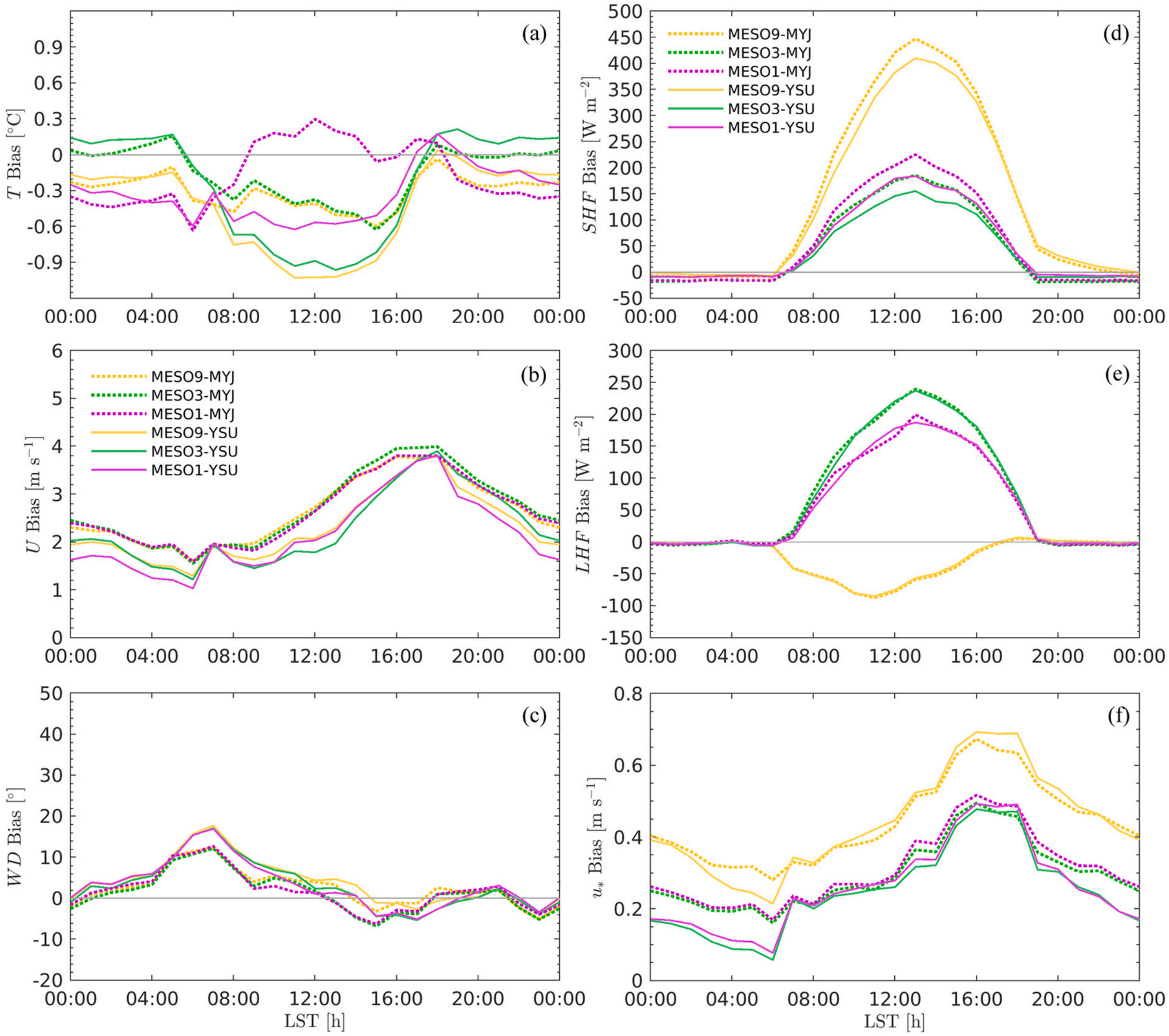

Fig. A1. Mean diurnal variations of biases between MESO simulations and observations throughout the 1-month simulation period. (a–c) 2-m temperature (*T*), 10-m wind speed (*U*), and wind direction (*WD*), which are averaged from AWS sites S1–S4; (d–f) surface sensible heat flux (*SHF*), latent heat flux (*LHF*), and friction velocity (u_*) at the EC site S5.

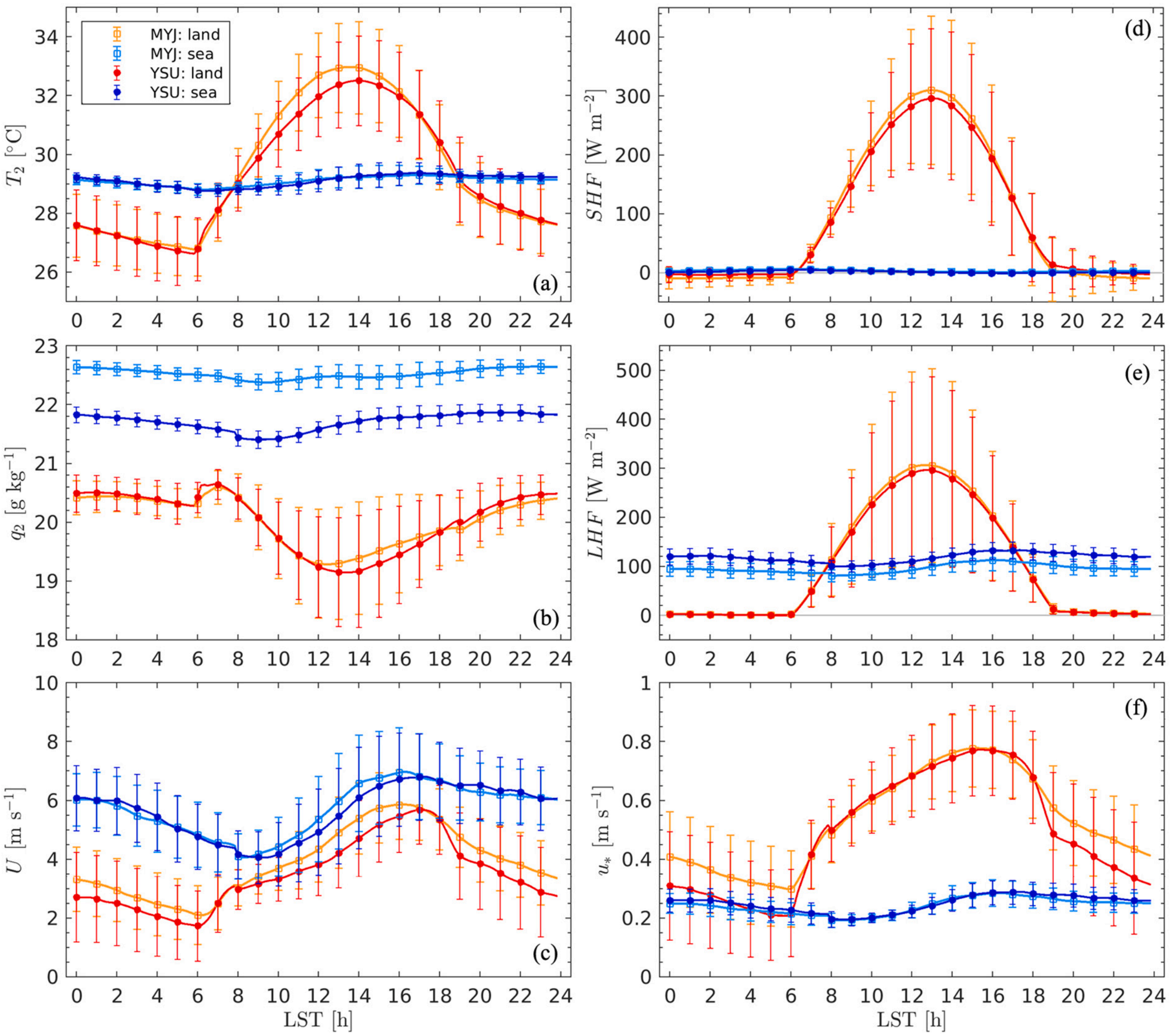

Fig. A2. Mean diurnal variations of near-surface meteorological variables over the land and sea in MESO1 during July 2020. (a–c) 2-m temperature (T_2), 2-m specific humidity (q_2), and 10-m wind speed (U); (d–f) surface sensible heat flux (SHF), latent heat flux (LHF), and friction velocity (u_*).

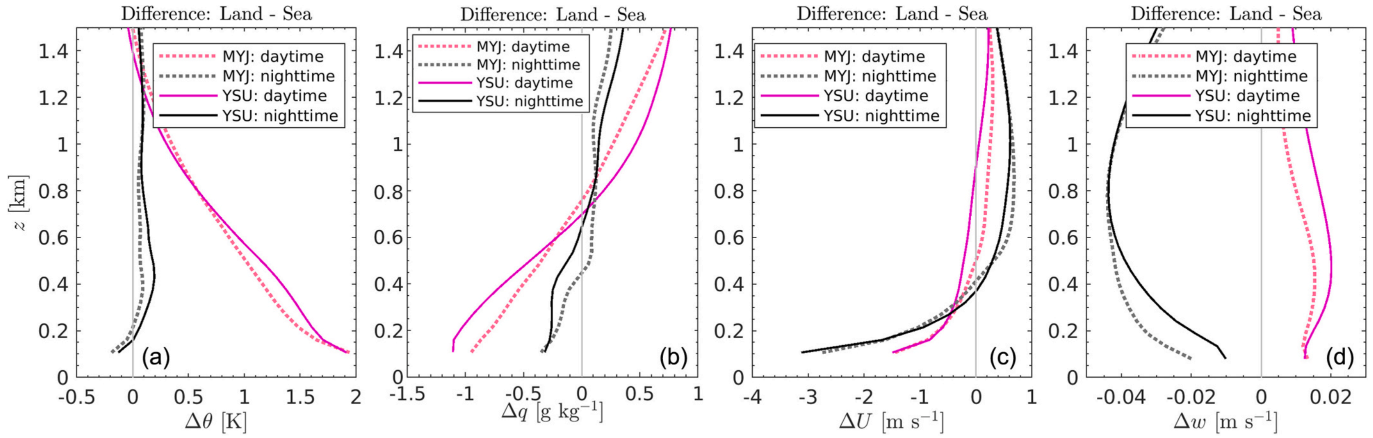

Fig. A3. Average differences of (a) potential temperature (θ), (b) specific humidity (q), (c) horizontal wind speed (U), and (d) vertical velocity (w) between land and sea simulated by the YSU and MYJ schemes during July 2020.

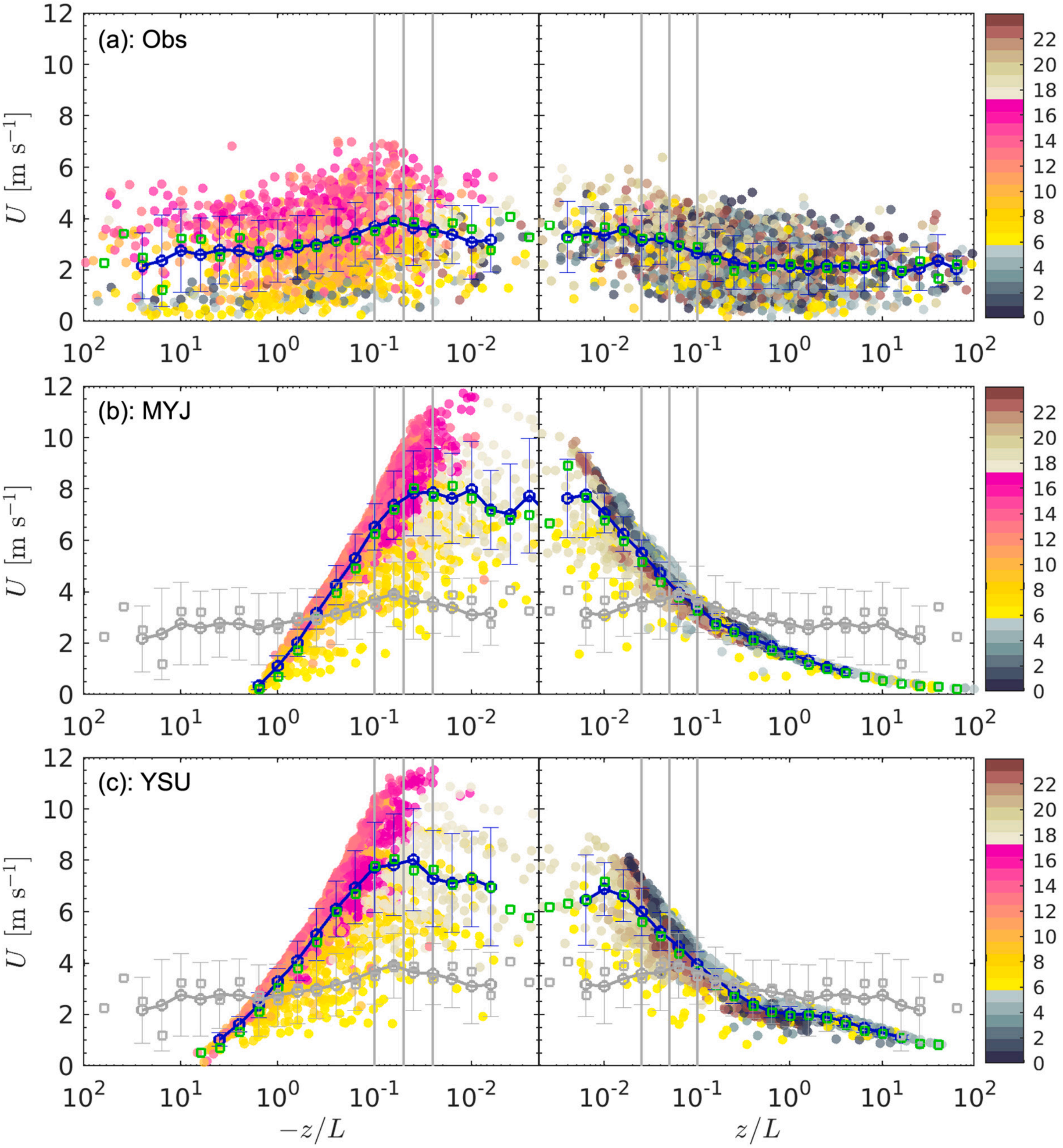

Fig. A4. Variations of 10-m wind speed (U) with atmospheric instability (z/L) for (a) observations, (b) simulations with the MYJ scheme, and (c) simulations with the YSU scheme. The colour bar indicates the local time in hours. The blue circles with error bars represent the corresponding bin averages and standard deviations, while the green squares denote the median values for bins. The gray circles and squares in (b, c) are bin averages and medians of observations from (a). The vertical gray lines are ±0.025, ±0.05, and ±0.1 lines of z/L. (For interpretation of the references to colour in this figure legend, the reader is referred to the web version of this article.)

References

Acevedo, O.C., Fitzjarrald, D.R., 2001. The early evening surface-layer transition: Temporal and spatial variability. J. Atmos. Sci. 58, 2650–2667. https://doi.org/10.1175/1520-0469(2001)058<2650:TEESLT>2.0.CO;2.

Aubinet, M., Vesala, T., Papale, D., 2012. Eddy Covariance: A Practical Guide to Measurement and Data Analysis. Springer, Dordrecht. https://doi.org/10.1007/978-94-007-2351-1.

Banks, R.F., Baldasano, J.M., 2016. Impact of WRF model PBL schemes on air quality simulations over Catalonia, Spain. Sci. Total Environ. 572, 98–113. https://doi.org/10.1016/j.scitotenv.2016.07.167.

Bian, L., Gao, Z., Ma, Y., Koike, T., Ma, Y., Li, Y., Sun, J., Hu, Z., Xu, X., 2012. Seasonal variation in turbulent fluxes over Tibetan Plateau and its surrounding areas: Research note. J. Meteorol. Soc. Jpn. 90, 157–171. https://doi.org/10.2151/jmsj.2012-C11.

Bonin, T., Chilson, P., Zielke, B., Fedorovich, E., 2013. Observations of the early evening boundary-layer transition using a small unmanned aerial system. Bound.-Layer Meteorol. 146, 119–132. https://doi.org/10.1007/s10546-012-9760-3.

Bretherton, C.S., Park, S., 2009. A new moist turbulence parameterization in the Community Atmosphere Model. J. Clim. 22, 3422–3448. https://doi.org/10.1175/2008JCLI2556.1.

Chen, F., Dudhia, J., 2001. Coupling an advanced land surface–hydrology model with the Penn State–NCAR MM5 modeling system. Part I: model implementation and sensitivity. Mon. Weather Rev. 129, 569–585. https://doi.org/10.1175/1520-0493(2001)129<0569:CAALSH>2.0.CO;2.

Cohen, A.E., Cavallo, S.M., Coniglio, M.C., Brooks, H.E., 2015. A review of planetary boundary layer parameterization schemes and their sensitivity in simulating southeastern US cold season severe weather environments. Weather Forecast. 30, 591–612. https://doi.org/10.1175/WAF-D-14-00105.1.

Coronel, R., Sawada, M., Iwasaki, T., 2016. Impacts of surface drag coefficient and planetary boundary layer schemes on the structure and energetics of typhoon Megi (2010) during intensification. J. Meteorol. Soc. Jpn. 94, 55–73. https://doi.org/10.2151/jmsj.2016-004.

Danielson, J.J., Gesch, D.B., 2011. Global multi-resolution terrain elevation data 2010 (GMTED2010). In: Technical Report 2011–1073. U.S. Geological Survey. Reston, Virginia. https://doi.org/10.3133/ofr20111073.

Falasca, S., Gandolfi, I., Argentini, S., Barnaba, F., Casasanta, G., Di Liberto, L., Petenko, I., Curci, G., 2021. Sensitivity of near-surface meteorology to PBL schemes in WRF simulations in a port-industrial area with complex terrain. Atmos. Res. 264, 105824 https://doi.org/10.1016/j.atmosres.2021.105824.

Friedl, M.A., Sulla-Menashe, D., Tan, B., Schneider, A., Ramankutty, N., Sibley, A., Huang, X., 2010. MODIS Collection 5 global land cover: Algorithm refinements and characterization of new datasets. Remote Sens. Environ. 114, 168–182. https://doi.org/10.1016/j.rse.2009.08.016.

Garratt, J.R., 1994. The atmospheric boundary layer. Earth Sci. Rev. 37, 89–134. https://doi.org/10.1016/0012-8252(94)90026-4.

He, J., Li, Q., Chan, P., Li, L., Lu, C., Zhang, L., Yang, H., 2021. Characteristics and vertical profiles of mean wind and turbulence for typhoon, monsoon, and thunderstorm winds. J. Struct. Eng. 147, 04021188. https://doi.org/10.1061/(ASCE)ST.1943-541X.0003156.

Hersbach, H., Bell, B., Berrisford, P., Biavati, G., Horányi, A., Muñoz Sabater, J., Nicolas, J., Peubey, C., Radu, R., Rozum, I., Schepers, D., Simmons, A., Soci, C., Dee, D., Thépaut, J.N., 2018a. ERA5 Hourly Data on Pressure Levels from 1959 to Present. https://doi.org/10.24381/cds.bd0915c6. URL. `https://cds.climate.copernicus.eu/cdsapp#!/dataset/10.24381/cds.bd0915c6?tab=overview`.

Hersbach, H., Bell, B., Berrisford, P., Biavati, G., Horányi, A., Muñoz Sabater, J., Nicolas, J., Peubey, C., Radu, R., Rozum, I., Schepers, D., Simmons, A., Soci, C., Dee, D., Thépaut, J.N., 2018b. ERA5 Hourly Data on Single Levels from 1959 to Present. https://doi.org/10.24381/cds.adbb2d47. URL. `https://cds.climate.copernicus.eu/cdsapp#!/dataset/reanalysis-era5-single-levels?tab=overview`.

Hong, S.Y., Lim, J.O.J., 2006. The WRF single-moment 6-class microphysics scheme (WSM6). Asia-Pac. J. Atmos. Sci. 42, 129–151.

Hong, S.Y., Pan, H.L., 1996. Nonlocal boundary layer vertical diffusion in a medium-range forecast model. Mon. Weather Rev. 124, 2322–2339. https://doi.org/10.1175/1520-0493(1996)124<2322:NBLVDI>2.0.CO;2.

Hong, S.Y., Noh, Y., Dudhia, J., 2006. A new vertical diffusion package with an explicit treatment of entrainment processes. Mon. Weather Rev. 134, 2318–2341. https://doi.org/10.1175/MWR3199.1.

Hu, X.M., Nielsen-Gammon, J.W., Zhang, F., 2010. Evaluation of three planetary boundary layer schemes in the WRF model. J. Appl. Meteorol. Climatol. 49, 1831–1844. https://doi.org/10.1175/2010JAMC2432.1.

Iacono, M.J., Delamere, J.S., Mlawer, E.J., Shephard, M.W., Clough, S.A., Collins, W.D., 2008. Radiative forcing by long-lived greenhouse gases: Calculations with the AER radiative transfer models. J. Geophys. Res. Atmos. 113, D13103. https://doi.org/10.1029/2008JD009944.

Jandaghian, Z., Touchaei, A.G., Akbari, H., 2018. Sensitivity analysis of physical parameterizations in WRF for urban climate simulations and heat island mitigation in Montreal. Urban Clim. 24, 577–599. https://doi.org/10.1016/j.uclim.2017.10.004.

Janjić, Z.I., 1994. The step-mountain eta coordinate model: further developments of the convection, viscous sublayer, and turbulence closure schemes. Mon. Weather Rev. 122, 927–945. https://doi.org/10.1175/1520-0493(1994)122<0927:TSMECM>2.0.CO;2.

Janjić, Z.I., 2002. Nonsingular implementation of the Mellor-Yamada level 2.5 scheme in the NCEP Meso model. In: NCEP Office Note 437. National Centers for Environmental Prediction. Washington DC, USA. URL: `https://repository.library.noaa.gov/view/noaa/11409`.

Jankov, I., Gallus, W.A., Segal, M., Shaw, B., Koch, S.E., 2005. The impact of different WRF model physical parameterizations and their interactions on warm season MCS rainfall. Weather Forecast. 20, 1048–1060. https://doi.org/10.1175/WAF888.1.

Jia, W., Zhang, X., 2020. The role of the planetary boundary layer parameterization schemes on the meteorological and aerosol pollution simulations: a review. Atmos. Res. 239, 104890 https://doi.org/10.1016/j.atmosres.2020.104890.

Jiménez, P.A., Dudhia, J., González-Rouco, J.F., Navarro, J., Montávez, J.P., García-Bustamante, E., 2012. A revised scheme for the WRF surface layer formulation. Mon. Weather Rev. 140, 898–918. https://doi.org/10.1175/MWR-D-11-00056.1.

Kaimal, J.C., Finnigan, J.J., 1994. Atmospheric Boundary Layer Flows: Their Structure and Measurement. Oxford University Press, Oxford, UK. https://doi.org/10.1093/oso/9780195062397.001.0001.

Konor, C.S., Boezio, G.C., Mechoso, C.R., Arakawa, A., 2009. Parameterization of PBL processes in an atmospheric general circulation model: description and preliminary assessment. Mon. Weather Rev. 137, 1061–1082. https://doi.org/10.1175/2008MWR2464.1.

Ma, Y., 2012. Evaluation of Polar WRF Simulations of Antarctic Atmospheric Circulation (in Chinese). Phd thesis.. Chinese Academy of Meteorological Sciences, Beijing, China.

Ma, Y.F., Pedersen, J., Grabowski, W., Kopec, M., Malinowski, S., 2018. Influences of subsidence and free-tropospheric conditions on the nocturnal growth of nonclassical marine stratocumulus. J. Adv. Model. Earth Syst. 10, 2706–2730. https://doi.org/10.1029/2018MS001295.

Mahrt, L., 1981. The early evening boundary layer transition. Q. J. R. Meteorol. Soc. 107, 329–343. https://doi.org/10.1002/qj.49710745205.

Malečić, B., Prtenjak, M.T., Horvath, K., Jelić, D., Jurković, P.M., Ćorko, K., Mahović, N. S., 2022. Performance of HAILCAST and the lightning potential index in simulating hailstorms in Croatia in a mesoscale model–Sensitivity to the PBL and microphysics parameterization schemes. Atmos. Res. 272, 106143 https://doi.org/10.1016/j.atmosres.2022.106143.

Mellor, G.L., Yamada, T., 1982. Development of a turbulence closure model for geophysical fluid problems. Rev. Geophys. 20, 851–875. https://doi.org/10.1029/RG020i004p00851.

Milovac, J., Warrach-Sagi, K., Behrendt, A., Späth, F., Ingwersen, J., Wulfmeyer, V., 2016. Investigation of PBL schemes combining the WRF model simulations with scanning water vapor differential absorption lidar measurements. J. Geophys. Res. Atmos. 121, 624–649. https://doi.org/10.1002/2015JD023927.

Misenis, C., Zhang, Y., 2010. An examination of sensitivity of WRF/Chem predictions to physical parameterizations, horizontal grid spacing, and nesting options. Atmos. Res. 97, 315–334. https://doi.org/10.1016/j.atmosres.2010.04.005.

Monin, A.S., Obukhov, A.M., 1954. Basic laws of turbulent mixing in the surface layer of the atmosphere. Tr. Akad. Nauk SSSR Geophiz. Inst. 24, 163–187.

Pleim, J.E., 2007. A combined local and nonlocal closure model for the atmospheric boundary layer. Part I: Model description and testing. J. Appl. Meteorol. Climatol. 46, 1383–1395. https://doi.org/10.1175/JAM2539.1.

Pradhan, P., Liberato, M.L., Kumar, V., Rao, S., Ferreira, J., Sinha, T., 2019. Simulation of mid-latitude winter storms over the North Atlantic Ocean: impact of boundary layer parameterization schemes. Clim. Dyn. 53, 6785–6814. https://doi.org/10.1007/s00382-019-04962-3.

Román-Cascón, C., Lothon, M., Lohou, F., Hartogensis, O., Vila-Guerau de Arellano, J., Pino, D., Yagüe, C., Pardyjak, E.R., 2021. Surface representation impacts on turbulent heat fluxes in the Weather Research and Forecasting (WRF) model (v. 4.1.3). Geosci. Model Dev. 14, 3939–3967. https://doi.org/10.5194/gmd-14-3939-2021.

Ruiz, J.J., Saulo, C., Nogués-Paegle, J., 2010. Wrf model sensitivity to choice of parameterization over South America: Validation against surface variables. Mon. Weather Rev. 138, 3342–3355. https://doi.org/10.1175/2010MWR3358.1.

Santos, D.C., Nascimento, E.D.L., 2016. Numerical simulations of the South American low level jet in two episodes of MCSs: Sensitivity to PBL and convective parameterization schemes. Adv. Meteorol. 2016, 2812978. https://doi.org/10.1155/2016/2812978.

Sathyanadh, A., Prabha, T.V., Balaji, B., Resmi, E., Karipot, A., 2017. Evaluation of WRF PBL parameterization schemes against direct observations during a dry event over the Ganges valley. Atmos. Res. 193, 125–141. https://doi.org/10.1016/j.atmosres.2017.02.016.

Seibert, P., Beyrich, F., Gryning, S.E., Joffre, S., Rasmussen, A., Tercier, P., 2000. Review and intercomparison of operational methods for the determination of the mixing height. Atmos. Environ. 34, 1001–1027. https://doi.org/10.1016/S1352-2310(99)00349-0.

Serafin, S., Adler, B., Cuxart, J., De Wekker, S.F., Gohm, A., Grisogono, B., Kalthoff, N., Kirshbaum, D.J., Rotach, M.W., Schmidli, J., Stiperski, I., Večenaj, Ž., Zardi, D., 2018. Exchange processes in the atmospheric boundary layer over mountainous terrain. Atmosphere 9, 102. https://doi.org/10.3390/atmos9030102.

Sfyri, E., Rotach, M.W., Stiperski, I., Bosveld, F.C., Lehner, M., Obleitner, F., 2018. Scalar-flux similarity in the layer near the surface over mountainous terrain. Bound.-Layer Meteorol. 169, 11–46. https://doi.org/10.1007/s10546-018-0365-3.

Shao, Y., Liu, S., Schween, J.H., Crewell, S., 2013. Large-eddy atmosphere-land-surface modelling over heterogeneous surfaces: Model development and comparison with measurements. Bound.-Layer Meteorol. 148, 333–356. https://doi.org/10.1007/s10546-013-9823-0.

Shin, H.H., Dudhia, J., 2016. Evaluation of PBL parameterizations in WRF at subkilometer grid spacings: Turbulence statistics in the dry convective boundary layer. Mon. Weather Rev. 144, 1161–1177. https://doi.org/10.1175/MWR-D-15-0208.1.

Shin, H.H., Hong, S.Y., 2015. Representation of the subgrid-scale turbulent transport in convective boundary layers at gray-zone resolutions. Mon. Weather Rev. 143, 250–271. https://doi.org/10.1175/MWR-D-14-00116.1.

Skamarock, W.C., Klemp, J.B., Dudhia, J., Gill, D.O., Liu, Z., Berner, J., Wang, W., Powers, J.G., Duda, M.G., Barker, D.M., Huang, X.Y., 2019. A Description of the Advanced Research WRF Model Version 4.1. Technical Report NCAR/TN-556+STR. National Center for Atmospheric Research, Boulder, Colorado, USA. https://doi.org/10.5065/1dfh-6p97.

Stensrud, D.J., 2011. Parameterization Schemes: Keys to Understanding Numerical Weather Prediction Models. Cambridge University Press. https://doi.org/10.1017/CBO9780511812590.

Stensrud, D., Coniglio, M., Knopfmeier, K., Clark, A., 2015. Numerical models: model physics parameterization. In: Encyclopedia of Atmospheric Sciences, Second edition. Elsevier Inc., pp. 167–180. https://doi.org/10.1016/B978-0-12-382225-3.00493-X

Stoy, P.C., Mauder, M., Foken, T., Marcolla, B., Boegh, E., Ibrom, A., Arain, M.A., Arneth, A., Aurela, M., Bernhofer, C., Cescatti, D., van Gorsel, E., Kiely, G., Knohl, A., Margolis, H., McCaughey, H., Merbold, L., Montagnani, L., Papale, D., Reichstein, M., Spano, D., Vaccari, F., Varlagin, A., 2013. A data-driven analysis of energy balance closure across fluxnet research sites: the role of landscape scale heterogeneity. Agric. For. Meteorol. 171, 137–152. https://doi.org/10.1016/j.agrformet.2012.11.004.

Stull, R.B., 1988. An Introduction to Boundary Layer Meteorology. Springer, Dordrecht. https://doi.org/10.1007/978-94-009-3027-8.

Stull, R.B., 1991. Static stability–an update. Bull. Am. Meteorol. Soc. 72, 1521–1530. https://doi.org/10.1175/1520-0477(1991)072<1521:SSU>2.0.CO;2.

Sun, X., Holmes, H.A., Osibanjo, O.O., Sun, Y., Ivey, C.E., 2017. Evaluation of surface fluxes in the WRF model: case study for farmland in rolling terrain. Atmosphere 8, 197. https://doi.org/10.3390/atmos8100197.

Sun, J., Takle, E.S., Acevedo, O.C., 2020. Understanding physical processes represented by the Monin–Obukhov bulk formula for momentum transfer. Bound.-Layer Meteorol. 177, 69–95. https://doi.org/10.1007/s10546-020-00546-5.

Tastula, E.M., Vihma, T., Andreas, E.L., 2012. Evaluation of Polar WRF from modeling the atmospheric boundary layer over Antarctic sea ice in autumn and winter. Mon. Weather Rev. 140, 3919–3935. https://doi.org/10.1175/MWR-D-12-00016.1.

Tastula, E.M., Galperin, B., Dudhia, J., LeMone, M.A., Sukoriansky, S., Vihma, T., 2015. Methodical assessment of the differences between the QNSE and MYJ PBL schemes for stable conditions. Q. J. R. Meteorol. Soc. 141, 2077–2089. https://doi.org/10.1002/qj.2503.

Tiedtke, M., 1989. A comprehensive mass flux scheme for cumulus parameterization in large-scale models. Mon. Weather Rev. 117, 1779–1800. https://doi.org/10.1175/1520-0493(1989)117<1779:ACMFSF>2.0.CO;2.

Xie, B., Fung, J.C., Chan, A., Lau, A., 2012. Evaluation of nonlocal and local planetary boundary layer schemes in the WRF model. J. Geophys. Res. Atmos. 117, D12103. https://doi.org/10.1029/2011JD017080.

Yu, E., Bai, R., Chen, X., Shao, L., 2022. Impact of physical parameterizations on wind simulation with WRF v3.9.1.1 under stable conditions at planetary boundary layer gray-zone resolution: a case study over the coastal regions of North China. Geosci. Model Dev. 15, 8111–8134. https://doi.org/10.5194/gmd-15-8111-2022.

Yusup, Y., Liu, H., 2016. Effects of atmospheric surface layer stability on turbulent fluxes of heat and water vapor across the water–atmosphere interface. J. Hydrometeorol. 17, 2835–2851. https://doi.org/10.1175/JHM-D-16-0042.1.

Zhang, C., Wang, Y., Hamilton, K., 2011. Improved representation of boundary layer clouds over the Southeast Pacific in ARW-WRF using a modified Tiedtke cumulus parameterization scheme. Mon. Weather Rev. 139, 3489–3513. https://doi.org/10.1175/MWR-D-10-05091.1.

Zhang, B.H., Liu, S.H., Liu, H.P., Ma, Y.J., 2012. The effect of MYJ and YSU schemes on the simulation of boundary layer meteorological factors of WRF. Chin. J. Geophys. (In Chinese) 55, 2239–2248. https://doi.org/10.6038/j.issn.0001-5733.2012.07.010.

Zhou, B., Simon, J.S., Chow, F.K., 2014. The convective boundary layer in the terra incognita. J. Atmos. Sci. 71, 2545–2563. https://doi.org/10.1175/JAS-D-13-0356.1.